ORIGINAL ARTICLE



The 10-th order of accuracy of 'quadratic' elements for elastic heterogeneous materials with smooth interfaces and unfitted Cartesian meshes

A. Idesman¹ · B. Dey² · M. Mobin¹

Received: 18 November 2021 / Accepted: 23 May 2022 © The Author(s), under exclusive licence to Springer-Verlag London Ltd., part of Springer Nature 2022

Abstract

Recently, we have developed the optimal local truncation error method (OLTEM) for PDEs with homogeneous materials on regular and irregular domains and Cartesian meshes as well as OLTEM with simple 9-point stencils for the 2-D scalar time-dependent wave and heat equations for heterogeneous materials with irregular interfaces. Here, OLTEM is extended to a much more general case of a system of elastic PDEs for heterogeneous materials with smooth irregular interfaces and unfitted Cartesian meshes. We also use larger 25-point stencils that are similar to those for quadratic quadrilateral finite elements. The interface conditions on the interfaces where the jumps in material properties occur are added to the expression for the local truncation error and do not change the width of the stencils. There are no unknowns on interfaces between different materials; the structure of the global discrete equations is the same for homogeneous and heterogeneous materials. The calculation of the unknown stencil coefficients is based on the minimization of the local truncation error of the stencil equations and yields the optimal 10-th order of accuracy for OLTEM with the 25-point stencils on unfitted Cartesian meshes. This corresponds to the increase in accuracy by seven orders for OLTEM compared to conventional quadratic finite elements with similar stencils. A new post-processing procedure for the stress calculations has been developed. Similar to basic computations, it includes OLTEM with the 25-point compact stencils and provides a very high accuracy of the stresses. Numerical experiments for elastic heterogeneous materials with circular and elliptical interfaces show that at the same number of degrees of freedom, OLTEM with unfitted meshes is more accurate than high order (up to the fifth order—the maximum order implemented in the COMSOL software) finite elements with a much greater stencil width and conformed meshes. Moreover, OLTEM with the 25-point stencils provides very accurate results for nearly incompressible materials (e.g., with Poisson ratio 0.4995).

Keywords Elasticity equations for heterogeneous materials \cdot Smooth interfaces \cdot Local truncation error \cdot Unfitted Cartesian meshes \cdot Optimal accuracy \cdot Compressible and nearly incompressible materials

1 Introduction

The finite element method, the finite volume method, the isogeometric elements, the spectral elements and similar techniques represent very powerful tools for the solution of partial differential equations (PDEs) for a complex geometry. However, the generation of non-uniform meshes for a complex geometry is not simple and may lead to the

decrease in accuracy of these techniques if 'bad' elements (e.g., elements with small angles) appear in the mesh. Moreover, the conventional derivation of discrete equations for these techniques (e.g., based on the Galerkin approaches) does not lead to the optimal accuracy of discrete equations. There is a significant number of publications related to the numerical solution of different PDEs on irregular domains with uniform embedded meshes. For example, we can mention the following fictitious domain numerical methods that use uniform embedded meshes: the embedded finite difference method, the cut finite element method, the finite cell method, the Cartesian grid method, the immersed interface method, the virtual boundary method, the embedded boundary method, etc.; e.g., see [1–30] and many others. The main objective of these techniques is to simplify the

Published online: 26 June 2022

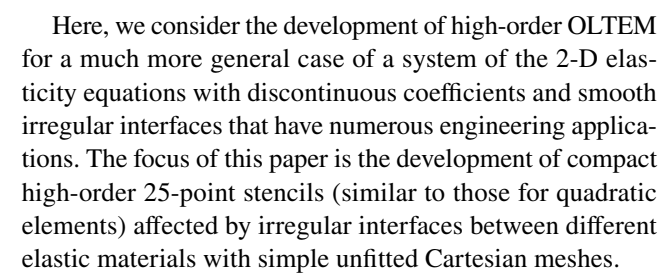


Department of Mechanical Engineering, Texas Tech University, Lubbock, TX 79409-1021, USA

Microvast Power Solutions, Inc., Orlando, FL 32826, USA

mesh generation for irregular domains as well as to mitigate the effect of 'bad' elements. For example, the techniques based on the finite element formulations (such as the cut finite element method, the finite cell method, the virtual boundary method and others) yield the p + 1 order of accuracy even with small cut cells generated due to complex irregular boundaries (e.g., see [2-5, 9, 28, 29] and many others). The main advantage of the embedded boundary method developed in [10–12, 24, 25] is the use of simple Cartesian meshes. The boundary conditions or fluxes in this technique are interpolated using the Cartesian grid points and this leads to the increase in the stencil width for the grid points located close to the boundary (the numerical techniques developed in [10–12, 24, 25] provide just the second order of accuracy for the global solution). A stable generalized finite element method for the Poisson equation was developed in [31] for heterogeneous materials with curved interfaces and unfitted uniform meshes. The second order of accuracy in the energy norm was achieved in [31] with 2-D quadratic finite elements that form 25-point stencils. The development of different numerical techniques (finite difference method, immersed finite element method, immersed meshfree method) for elasticity interface problems with unfitted meshes were recently reported in [32–34]. The development of robust numerical techniques for the solution of PDEs for heterogeneous materials with complex irregular interfaces that provide an optimal accuracy on simple unfitted meshes is still a challenging problem.

Recently in our papers [35-41], we have developed OLTEM for the solution of PDEs with constant coefficients (homogeneous materials) on regular and irregular domains with Cartesian meshes. At the same structure of the semidiscrete or discrete equations, the new technique provides the optimal order of accuracy that exceeds the order of accuracy of many known numerical approaches on regular and irregular domains. For example, in our paper [38], we showed that OLTEM with nine-point stencils (similar to those for linear finite elements) provides the second order of accuracy for the 2-D elasticity on regular domains. The second order of accuracy is the optimal accuracy for all ninepoint stencils independent of the numerical method used for their derivations. The paper [38] also shows that OLTEM with 25-point stencils (similar to those for quadratic finite elements) provides the 10-th order of accuracy for the 2-D elasticity on regular domains and conformed meshes. In our paper [42], we have extended OLTEM with 9-point stencils (similar to those for linear finite elements) and unfitted Cartesian meshes to the 2-D time-dependent scalar heat and wave equations with discontinuous coefficients and we have obtained the third order of accuracy of the new approach.



In Sect. 2.2, OLTEM with 25-point compact stencils for the 2-D elasticity equations is derived for heterogeneous materials with zero body forces. Its extension to nonzero body forces is considered in Sect. 2.3. Section 3 presents the derivation of a new post-processing procedure for stress calculation. 2-D numerical examples for compressible and near incompressible heterogeneous materials with circular and elliptical interfaces as well as the comparison with FEM are presented in Sect. 4. Concluding remarks are given in Sect. 5. For the derivation of many analytical expressions presented below, we use the computational program "Mathematica". We also used the 'ToMatlab' package for the conversion of 'Mathematica' expressions to a Matlab code.

2 OLTEM with 25-point stencils for the 2-D elasticity equations with discontinuous material properties

In this section, we first introduce the elasticity equations for heterogeneous materials and the local truncation error. Then, we derive OLTEM with 25-point stencils for heterogeneous elastic materials with irregular interfaces in the case of zero body forces. Finally, we take into account nonzero body forces.

2.1 Elasticity equations and the local truncation error

The 2-D time-independent elasticity equations in a composite domain $\Omega = \bigcup \Omega_l$ ($l = 1, 2, ..., \bar{N}$ where \bar{N} is the total number of subdomains) can be written down in each subdomain Ω_l as follows:

$$\mu_{l}\nabla^{2}u_{l} + (\mu_{l} + \lambda_{l})\left(\frac{\partial^{2}u_{l}}{\partial x^{2}} + \frac{\partial^{2}v_{l}}{\partial x \partial y}\right) + f_{x}^{l} = 0,$$

$$\mu_{l}\nabla^{2}v_{l} + (\mu_{l} + \lambda_{l})\left(\frac{\partial^{2}v_{l}}{\partial y^{2}} + \frac{\partial^{2}u_{l}}{\partial x \partial y}\right) + f_{y}^{l} = 0,$$

$$(1)$$

where $u_l = u_l(x, y)$ and $v_l = v_l(x, y)$ are the x- and y-components of the displacement vector, $f_x^l = f_x^l(x, y)$ and $f_y^l = f_y^l(x, y)$ are the x- and y-components of the body forces that can be discontinuous across interfaces, μ_l and λ_l are



Lame coefficients that can be also expressed in terms of Young's modulus E and Poisson's ratio ν as follows:

$$\mu_l = \frac{E_l}{2(1+v_l)}, \quad \lambda_l = \frac{E_l v_l}{(1+v_l)(1-2v_l)}.$$
 (2)

We also assume that the functions u_l and f_l are sufficiently smooth in each subdomain Ω_l . At the interface G between any two subdomains, the following interface conditions (the continuity of the displacements and the tractive forces across the interface) are applied:

$$u_G^* - u_G^{**} = 0, \quad v_G^* - v_G^{**} = 0,$$
 (3)

$$t_{x,G}^* - t_{x,G}^{**} = 0, \quad t_{y,G}^* - t_{y,G}^{**} = 0,$$
 (4)

where the symbols * and ** correspond to the quantities on the opposite sides from the interface for the corresponding subdomains Ω_l . The x- and y-components of the tractive forces $t_{x,G}$ and $t_{y,G}$ can be expressed in terms of the displacements as follows:

$$t_{x,G} = n_x \left[(\lambda + 2\mu) \frac{\partial u}{\partial x} + \lambda \frac{\partial v}{\partial y} \right] + n_y \mu \left(\frac{\partial u}{\partial y} + \frac{\partial v}{\partial x} \right),$$

$$t_{y,G} = n_y \left[(\lambda + 2\mu) \frac{\partial v}{\partial y} + \lambda \frac{\partial u}{\partial x} \right] + n_x \mu \left(\frac{\partial u}{\partial y} + \frac{\partial v}{\partial x} \right),$$
(5)

where n_x and n_y are the x- and y-components of the normal vector at the interface. According to Eqs. (3)–(5), the displacements u and v are continuous across the interfaces but they can have the discontinuous spatial derivatives across the interfaces. We should note that the derivation of the new approach can be easily extended to the case with the discontinuous displacements and tractive forces across interfaces; i.e., when the right-hand sides in Eqs. (3) and (4) are the given functions. However, for simplicity we consider Eqs. (3) and (4) with zero right-hand sides. We should also mention that despite the assumptions about the smoothness of the exact solutions solved by OLTEM, the numerical experiments (e.g., see our paper [36]) show that OLTEM also yields accurate results for non-smooth solutions.

In this paper, the Dirichlet boundary conditions $u = g_1$ and $v = g_2$ are applied along the external boundary Γ where g_1 and g_2 are the given functions. However, the Neumann boundary conditions (tractive forces) can be also used with the proposed approach; e.g., see our papers [40, 43]. According to OLTEM, the discrete system for the elasticity equations, Eq. (1), after the space discretization with a Cartesian rectangular mesh can be represented as a system of linear algebraic equations. The algebraic equations of this system for each internal grid point of the domain are called

the stencil equations. For the 2-D elasticity equations, two stencil equations can be written down for each grid point as follows:

$$\sum_{i=1}^{L} k_{j,i} u_i^{\text{num}} + \sum_{i=1}^{L} \bar{k}_{j,i} v_i^{\text{num}} = \bar{f}_j, \quad j = 1, 2,$$
 (6)

where u_i^{num} and v_i^{num} are the numerical solution for the displacements u and v at the i-th grid point, k_{ij} and \bar{k}_{ij} are the unknown stencil coefficients corresponding to the displacements u and v (they should be determined), L is the number of the grid points included into a stencil, \bar{f}_i are the components of the discretized body forces (see the next sections). Many numerical techniques such as the finite difference method, the finite element method, the finite volume method, the isogeometric elements, the spectral elements, different meshless methods and others can be finally reduced to Eq. (6) with some specific coefficients k_{ij} and \bar{k}_{ij} . To demonstrate a new technique, below we will assume compact 25-point stencils (L = 25) in the 2-D case that correspond to the width of the stencils for quadratic quadrilateral finite elements on Cartesian meshes and that require similar computational costs as those for quadratic finite elements. However, the stencils with any width can be used with the suggested approach.

Let us introduce the local truncation error used with OLTEM. The replacement of the numerical values of the displacements u_i^{num} and v_i^{num} at the grid points in Eq. (6) by the exact solution u_i and v_i to the elasticity equations, Eq. (1), leads to the residual of these equations called the local truncation error e_i of the discrete equations, Eq. (6):

$$e_j = \sum_{i=1}^{L} k_{j,i} u_i + \sum_{i=1}^{L} \bar{k}_{j,i} v_i - \bar{f}_j, \quad j = 1, 2.$$
 (7)

Calculating the difference between Eqs. (7) and (6) we can get

$$e_{j} = \sum_{i=1}^{L} \{k_{j,i}[u_{i} - u_{i}^{\text{num}}] + \bar{k}_{j,i}[v_{i} - v_{i}^{\text{num}}]\}$$

$$= \sum_{i=1}^{L} (k_{j,i}\bar{e}_{i} + \bar{k}_{j,i}\bar{e}_{i}^{*}), \quad j = 1, 2,$$
(8)

where $\bar{e}_i = u_i - u_i^{\text{num}}$ and $\bar{e}_i^* = v_i - v_i^{\text{num}}$ are the errors in the displacements u and v at the grid point i. As can be seen from Eq. (8), the local truncation errors e_j (j = 1, 2) are a linear combination of the errors in the displacements u and v at the grid points which are included into the stencil equations.



2.2 Zero body forces $f_x^l = 0$ and $f_y^l = 0$ in Eq. (1)

2.2.1 25-point stencils with and without interface

Let us consider a 2-D bounded domain and a Cartesian rectangular mesh with a mesh size h where h is the size of the mesh along the x-axis, $b_y h$ is the size of the mesh along the y-axis (b_y is the aspect ratio of the mesh). To simplify derivations, below we consider rectangular domains with irregular interfaces between different materials. However, irregular domains can be also considered with OLTEM; see [35–37]. Here, we will develop 25-point uniform stencils that provide the tenth order of accuracy. We should mention that we use the same structure of stencils for homogeneous and heterogeneous materials (the difference between homogeneous and heterogeneous materials is in the values of the stencil coefficients only). The spatial locations of the 24 grid points that are close to the central grid point with (u_{13}, v_{13}) and contribute to the 25-point stencil for the central grid point are shown in Fig. 1. For convenience, the local numeration of the grid points from 1 to 25 is used in Fig. 1 as well as in the derivations below. The interface in Fig. 1b divides the 25-point uniform stencil into two parts with different material properties. To impose the interface conditions at the interface, we select a small number of interface points as follows. First, we select one point at the interface with the coordinates $x_G = x_{G,1}$ and $y_G = y_{G,1}$. This point can be selected as the shortest distance from the central grid point (u_{13}, v_{13}) of the 25-point stencil to the interface. Then, we additionally select n interface points to the left and to the right from the point with the coordinates $x_{G,1}$ and $y_{G,1}$ at the same distances $\bar{h} = \sqrt{(x_{G,i+1} - x_{G,i})^2 + (y_{G,i+1} - y_{G,i})^2}$ $(i = 1, 2, \dots, 2n)$ from each other; e.g., see Fig. 1b for 25-point stencils. The numerical experiments show that small distances $\bar{h} = h/5$ between the selected interface points yield accurate results. The total number of selected interface points is $N_G = 2n + 1$ where $N_G = 9$ is used for the 25-point stencils developed below.

Let us describe the coordinates of the grid points of the 25-point uniform stencil (see Fig. 1) with respect to the central grid point (x_{13}, y_{13}) as follows:

$$x_p = x_{13} + (i-3)h, \quad y_p = y_{13} + (j-3)b_yh,$$
 (9)

for the 25-point stencils where p = 5(j - 1) + i with i, j = 1, 2, 3, 4, 5.

To describe the coordinates of the selected N_G points on the interface (see Fig. 1b), we introduce $2(N_G-1)$ coefficients $d_{x,p}$ and $d_{y,p}$ ($p=2,3,\ldots,N_G$) as follows (see also Fig. 1b):

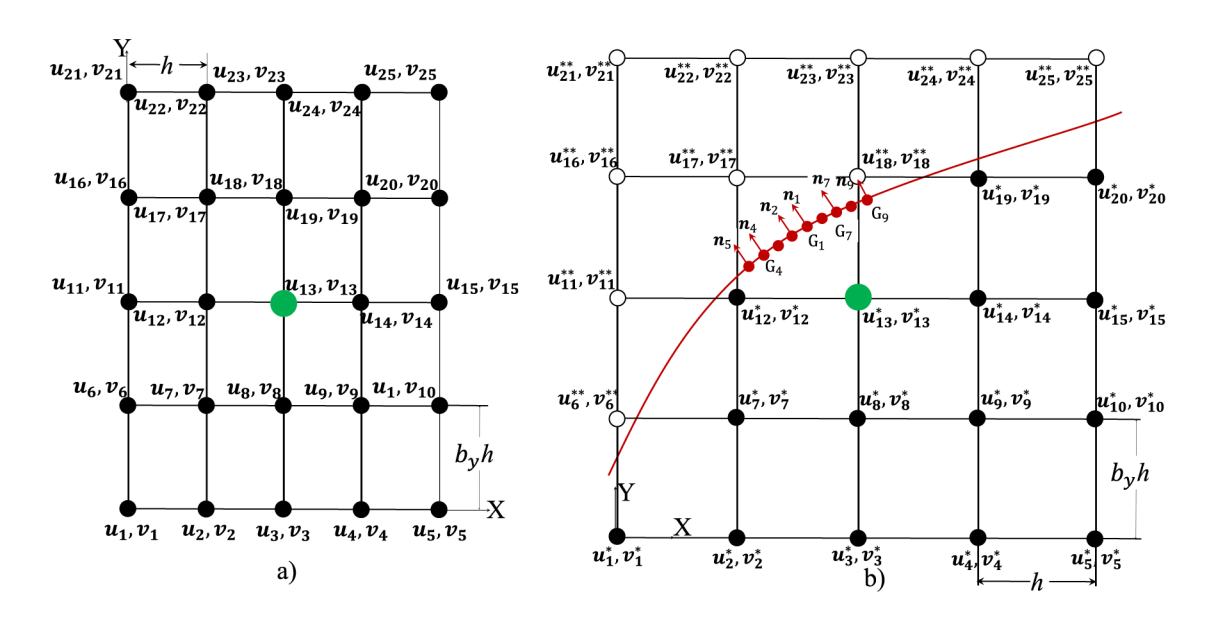


Fig. 1 The spatial locations of the degrees of freedom u_p and v_p (p = 1, 2, ..., 25) that contribute to the 25-point uniform stencil for the internal degrees of freedom u_{13} and v_{13} for homogeneous material without interface (**a**) and for heterogeneous material with interface (**b**)



$$x_{G,m} = x_G + d_{x,m}h,$$

 $y_{G,m} = y_G + d_{y,m}b_yh, \quad m = 2, 3, ..., N_G.$ (10)

For the proposed approach, some interface points G_m $(m=1,2,\ldots,N_G)$ can be located slightly outside the 25-point cell. The derivations presented below are also valid for these cases.

The stencil equations, Eq. (6), for heterogeneous materials with the 25-point uniform stencil for the grid point (x_{13}, y_{13}) (see Fig. 1b) will be assumed in the following form:

$$\sum_{p=1}^{25} k_{j,p} [a_p u_p^{*,\text{num}} + (1 - a_p) u_p^{**,\text{num}}] + \sum_{p=1}^{25} \bar{k}_{j,p} [a_p v_p^{*,\text{num}} + (1 - a_p) v_p^{**,\text{num}}] = \bar{f}_{i,13}, \quad j = 1, 2,$$
(11)

where $\bar{f}_{j,13}=0$ in the case of zero body forces $f_x^l=f_y^l=0$ in Eq. (1), the unknown coefficients $k_{j,p}$ and $\bar{k}_{j,p}$ ($p=1,2,\ldots,25$) are to be determined from the minimization of the local truncation error, the coefficients $a_p=1$ if the grid point u_p belongs to material * or $a_p=0$ if the grid point u_p belongs to another material ** (i.e., only two variables $u_p^{*,\text{num}}$, $v_p^{*,\text{num}}$ or $u_p^{**,\text{num}}$, $v_p^{**,\text{num}}$ are included into Eq. (11) for each grid point; e.g., see Fig. 1b with $a_i=1$ (i=1,2,3,4,5,7,8,9,10,12,13,14,15,19,20) and $a_j=0$ (j=6,11,16,17,18,21,22,23,24,25)).

We should note that usually the stencil equations similar to Eq. (11) include the coefficient h^2 in the denominator in order to express the second space derivatives in the elasticity equations, Eq. (1). However, for convenience, the stencil equations, Eq. (11), are multiplied by h^2 to write down them without $\frac{1}{h^2}$. Therefore, the expressions for the local truncation error used in the paper are also multiplied by h^2 .

2.2.2 The local truncation error for 25-point stencils with interface

The local truncation error e_j follows from Eq. (11) by the replacement of the numerical solution $u_p^{*,\text{num}}, u_p^{**,\text{num}}, v_p^{*,\text{num}}$ and $v_p^{**,\text{num}}$ by the exact solution u_p^*, u_p^{**}, v_p^* and v_p^{**} :

$$e_{j} = \sum_{p=1}^{25} k_{j,p} [a_{p}u_{p}^{*} + (1 - a_{p})u_{p}^{**}] + \sum_{p=1}^{25} \bar{k}_{j,p} [a_{p}v_{p}^{*} + (1 - a_{p})v_{p}^{**}] - \bar{f}_{j,13}, \quad j = 1, 2.$$

$$(12)$$

One of the ideas of the new approach is to include the interface conditions for the exact solution at a small number of the selected interface points into Eq. (12) for the local truncation error as follows:

$$e_{j} = \sum_{p=1}^{25} k_{j,p} [a_{p}u_{p}^{*} + (1 - a_{p})u_{p}^{**}]$$

$$+ \sum_{p=1}^{25} \bar{k}_{j,p} [a_{p}v_{p}^{*} + (1 - a_{p})v_{p}^{**}]$$

$$+ \sum_{m=1}^{N_{G}} q_{1,m} (u_{G,m}^{*} - u_{G,m}^{**}) + \sum_{m=1}^{N_{G}} q_{2,m} (v_{G,m}^{*} - v_{G,m}^{**})$$

$$+ \sum_{m=1}^{N_{G}} hq_{3,m} \left\{ \left[n_{x,m} \left[(\lambda_{*} + 2\mu_{*}) \frac{\partial u_{G,m}^{*}}{\partial x} + \lambda_{*} \frac{\partial v_{G,m}^{*}}{\partial y} \right] \right.$$

$$+ n_{y,m} \mu_{*} \left(\frac{\partial u_{G,m}^{**}}{\partial y} + \frac{\partial v_{G,m}^{**}}{\partial x} \right) \right]$$

$$- \left[n_{x,m} \left[(\lambda_{**} + 2\mu_{**}) \frac{\partial u_{G,m}^{**}}{\partial x} + \lambda_{**} \frac{\partial v_{G,m}^{**}}{\partial y} \right] \right.$$

$$+ n_{y,m} \mu_{**} \left(\frac{\partial u_{G,m}^{**}}{\partial y} + \frac{\partial v_{G,m}^{**}}{\partial x} \right) \right]$$

$$+ n_{x,m} \mu_{*} \left(\frac{\partial u_{G,m}^{*}}{\partial y} + \frac{\partial v_{G,m}^{*}}{\partial x} \right)$$

$$- \left[n_{y,m} \left[(\lambda_{**} + 2\mu_{**}) \frac{\partial v_{G,m}^{**}}{\partial y} + \lambda_{**} \frac{\partial u_{G,m}^{**}}{\partial x} \right]$$

$$+ n_{x,m} \mu_{**} \left(\frac{\partial u_{G,m}^{**}}{\partial y} + \frac{\partial v_{G,m}^{**}}{\partial x} \right) \right] \right\} - \bar{f}_{j,13}, \quad j = 1, 2,$$

$$(13)$$

where $n_{x,m}$ and $n_{y,m}$ are the x and y-components of the normal vectors at the selected N_G interface points (e.g., see Fig. 1b), the unknown coefficients $q_{1,m}$, $q_{2,m}$, $q_{3,m}$ and $q_{4,m}$ $(m = 1, 2, ..., N_G)$ will be used for the minimization of the local truncation error in Eq. (13), the expressions in parenthesis after $q_{1,m}$, $q_{2,m}$, $q_{3,m}$ and $q_{4,m}$ are the interface conditions at the selected N_G interface points and are equal to zero (see Eqs. (3)–(5)). Therefore, Eqs. (12) and (13) yield the same local truncation error e_i . The addition of the interface conditions at $N_G = 9$ points in Eq. (13) provides additional $4N_G = 36$ unknown coefficients $q_{1,m}$, $q_{2,m}$, $q_{3,m}$ and $q_{4,m}$ $(m = 1, 2, ..., N_G)$ that along with 50 unknown stencil coefficients $k_{i,p}$, $k_{i,p}$ (p = 1, 2, ..., 25) are used for the minimization of the local truncation error; see below Eq. (27). This allows us to get the tenth order of accuracy of OLTEM for general geometry of interfaces; see below.



Remark 1 In Eq. (13), we consider two local truncation errors for the first j = 1 and second j = 2 stencils. The coefficients $q_{1,m}$, $q_{2,m}$, $q_{3,m}$ and $q_{4,m}$ $(m = 1, 2, ..., N_G)$ are different for these two stencils. However, in order to simplify the notations we omit index j for the coefficients $q_{1,m}$, $q_{2,m}$, $q_{3,m}$ and $q_{4,m}$.

2.2.3 The number of unknown stencil coefficients

Only $50 + 4N_G - 1$ out of the $50 + 4N_G$ coefficients $k_{i,p}$, $\bar{k}_{i,p}$, $q_{1,m}, q_{2,m}, q_{3,m}, q_{4,m} (p = 1, 2, ..., 25, m = 1, 2, ..., N_G)$ in Eq. (13) can be considered as unknown coefficients. This can be explained as follows. In the case of zero body forces $\bar{f}_{i,13} = 0$, Eq. (11) can be rescaled by the division of the left- and right-hand sides of Eq. (11) by any scalar, i.e., one of the coefficients can be selected as unity and there will be only $50 + 4N_G - 1$ unknown rescaled coefficients. The case of nonzero body forces $\bar{f}_{i,13} \neq 0$ can be similarly treated because the term $\bar{f}_{i,13}$ is a linear function of the stencil coefficients; see below. For convenience, we will scale the stencil coefficients in such a way that $k_{1.13}$ is $k_{1.13} = 1$. Moreover, similar to finite element stencils, we select $\bar{k}_{1,13} = 0$.

2.2.4 Taylor series of the local truncation error

To represent the local truncation error e_i as a Taylor series, let us expand the exact solution at the grid points and the selected N_G interface points in Eq. (13) into a Taylor series at small $h \ll 1$ in the vicinity of the central interface point (x_G, y_G) as follows:

$$c_{p} = c_{G} + \frac{\partial c_{G}}{\partial x} [((i-3) - dx_{G})h] + \frac{\partial c_{G}}{\partial y} [((l-3) - dy_{G})b_{y}h] + \frac{1}{\mu_{*}} \frac{\partial^{(i+j)}f_{G,y}^{*}}{\partial x^{i}\partial y^{j}}],$$

$$+ \frac{\partial^{2}c_{G}}{\partial x^{2}} \frac{[((i-3) - dx_{G})h]^{2}}{2!} + \frac{\partial^{2}c_{G}}{\partial y^{2}} \frac{[((l-3) - dy_{G})b_{y}h]^{2}}{2!} + \cdots,$$

$$+ 2\frac{\partial^{2}c_{G}}{\partial x\partial y} \frac{[((i-3) - dx_{G})h][((l-3) - dy_{G})b_{y}h]}{2!} + \cdots,$$

$$p = 5(l-1) + i \quad \text{with } i, l = 1, 2, 3, 4, 5$$

$$+ s_{3}^{**} \frac{\partial^{(i+j)}f_{G,x}^{**}}{\partial x^{i}\partial y^{(2+j)}} + s_{2}^{***} \frac{\partial^{(2+i+j)}v_{G}^{***}}{\partial x^{(i+1)}\partial y^{(j+1)}} + s_{3}^{***} \frac{\partial^{(i+j)}f_{G,x}^{**}}{\partial x^{(i+1)}\partial y^{(j+1)}}$$

$$+ s_{3}^{***} \frac{\partial^{(i+j)}f_{G,x}^{**}}{\partial x^{(i+j)}\partial y^{(j+1)}} + s_{2}^{***} \frac{\partial^{(2+i+j)}v_{G}^{***}}{\partial x^{(i+1)}\partial y^{(j+1)}} + s_{3}^{***} \frac{\partial^{(i+j)}f_{G,x}^{***}}{\partial x^{(i+1)}\partial y^{(i+1)}} + s_{3}^{**} \frac{\partial^{(i+j)}f_{G,x}^{**}}{\partial x^{(i+1)}\partial y^{($$

$$w_{j} = w_{G} + \frac{\partial w_{G}}{\partial x} [d_{x,j}h] + \frac{\partial w_{G}}{\partial y} [d_{y,j}b_{y}h]$$

$$+ \frac{\partial^{2}w_{G}}{\partial x^{2}} \frac{[d_{x,j}h]^{2}}{2!} + \frac{\partial^{2}w_{G}}{\partial y^{2}} \frac{[d_{y,j}b_{y}h]^{2}}{2!}$$

$$+ 2 \frac{\partial^{2}w_{G}}{\partial x \partial y} \frac{[(d_{x,j}h)[d_{y,j}b_{y}h]}{2!} + \cdots, \quad j = 1, 2, \dots, 9,$$
(15)

with $dx_G = \frac{x_G - x_{13}}{h}$ and $dy_G = \frac{y_G - y_{13}}{b_v h}$. In Eq. (14) the function $\begin{array}{l} c_p \text{ is } u_p^*, u_p^{**}, v_p^*, v_p^{**}, v_p^{**} \text{ in Eq. (15) the function } w_j \text{ is } u_{G,j}^*, u_{G,j}^{**}, \\ \frac{\partial u_{G,j}^*}{\partial x}, \frac{\partial u_{G,j}^{**}}{\partial x}, \frac{\partial u_{G,j}^{**}}{\partial y}, \frac{\partial u_{G,j}^{**}}{\partial y}, v_{G,j}^{**}, v_{G,j}^{**}, \frac{\partial v_{G,j}^*}{\partial x}, \frac{\partial v_{G,j}^{**}}{\partial x}, \frac{\partial v_{G,j}^{**}}{\partial y}, \frac{\partial v_{G,j}^{**}}{\partial y}. \end{array}$ The exact solution u_G^* , u_G^{**} , v_G^* and v_G^{**} to the elasticity equations, Eq. (1), at the central interface point with the coordinates $x = x_G$ and $y = y_G$ meets the following equations:

$$\frac{\partial^{2} u_{G}^{*}}{\partial x^{2}} = -\left[s_{1}^{*} \frac{\partial^{2} u_{G}^{*}}{\partial y^{2}} + s_{2}^{*} \frac{\partial^{2} v_{G}^{*}}{\partial x \partial y} + s_{3}^{*} f_{G,x}^{*}\right],$$

$$\frac{\partial^{2} v_{G}^{*}}{\partial x^{2}} = -\left[\frac{1}{s_{1}^{*}} \frac{\partial^{2} v_{G}^{*}}{\partial y^{2}} + s_{4}^{*} \frac{\partial^{2} u_{G}^{*}}{\partial x \partial y} + \frac{1}{\mu_{*}} f_{G,y}^{*}\right],$$
(16)

$$\frac{\partial^{2} u_{G}^{**}}{\partial x^{2}} = -\left[s_{1}^{**} \frac{\partial^{2} u_{G}^{**}}{\partial y^{2}} + s_{2}^{**} \frac{\partial^{2} v_{G}^{**}}{\partial x \partial y} + s_{3}^{**} f_{G,x}^{**}\right],$$

$$\frac{\partial^{2} v_{G}^{**}}{\partial x^{2}} = -\left[\frac{1}{s_{1}^{**}} \frac{\partial^{2} v_{G}^{**}}{\partial y^{2}} + s_{4}^{**} \frac{\partial^{2} u_{G}^{**}}{\partial x \partial y} + \frac{1}{\mu_{**}} f_{G,y}^{**}\right],$$
(17)

$$\frac{\partial^{(2+i+j)} u_G^*}{\partial x^{(2+i)} \partial y^j} = -\left[s_1^* \frac{\partial^{(2+i+j)} u_G^*}{\partial x^i \partial y^{(2+j)}} + s_2^* \frac{\partial^{(2+i+j)} v_G^*}{\partial x^{(i+1)} \partial y^{(j+1)}} + s_3^* \frac{\partial^{(i+j)} f_{G,x}^*}{\partial x^i \partial y^j} \right],$$
(18)

$$\frac{\partial^{(2+i+j)}v_{G}^{*}}{\partial x^{(2+i)}\partial y^{j}} = -\left[\frac{1}{s_{1}^{*}}\frac{\partial^{(2+i+j)}v_{G}^{*}}{\partial x^{i}\partial y^{(2+j)}} + s_{4}^{*}\frac{\partial^{(2+i+j)}u_{G}^{*}}{\partial x^{(i+1)}\partial y^{(j+1)}} + \frac{1}{\mu_{*}}\frac{\partial^{(i+j)}f_{G,y}^{*}}{\partial x^{i}\partial y^{j}}\right],$$
(19)

$$\frac{\partial^{(2+i+j)} u_G^{**}}{\partial x^{(2+i)} \partial y^j} = -\left[s_1^{**} \frac{\partial^{(2+i+j)} u_G^{**}}{\partial x^i \partial y^{(2+j)}} + s_2^{**} \frac{\partial^{(2+i+j)} v_G^{**}}{\partial x^{(i+1)} \partial y^{(j+1)}} + s_3^{**} \frac{\partial^{(i+j)} f_{G,x}^{**}}{\partial x^i \partial y^j} \right],$$
(20)



$$\begin{split} \frac{\partial^{(2+i+j)}v_{G}^{**}}{\partial x^{(2+i)}\partial y^{j}} &= -\left[\frac{1}{s_{1}^{**}}\frac{\partial^{(2+i+j)}v_{G}^{**}}{\partial x^{i}\partial y^{(2+j)}} + s_{4}^{**}\frac{\partial^{(2+i+j)}u_{G}^{**}}{\partial x^{(i+1)}\partial y^{(j+1)}} \right. \\ &\quad + \frac{1}{\mu_{**}}\frac{\partial^{(i+j)}f_{G,y}^{**}}{\partial x^{i}\partial y^{j}}\right], \\ s_{1}^{*(**)} &= \frac{\mu_{*(**)}}{2\mu_{*(**)} + \lambda_{*(**)}}, \quad s_{2}^{*(**)} &= \frac{\mu_{*(**)} + \lambda_{*(**)}}{2\mu_{*(**)} + \lambda_{*(**)}}, \\ s_{3}^{*(**)} &= \frac{1}{2\mu_{*(**)} + \lambda_{*(**)}}, \quad s_{4}^{*(**)} &= \frac{\mu_{*(**)} + \lambda_{*(**)}}{\mu_{*(**)}}, \end{split}$$

with $i, j = 0, 1, 2, 3, 4, \dots$ We should mention that Eqs. (16) and (17) directly follow from Eq. (1) while Eqs. (18)–(21) are obtained by the differentiation of Eqs. (16) and (17) with respect to x and y.

2.2.5 The difference in the derivations for the first and second 25-point stencils

In Eqs. (16) and (17), we have expressed the second x derivatives in terms of the second y derivatives and the second mixed derivatives. However, similarly, we can express the second y derivatives in terms of the second x derivatives and the second mixed derivatives. This latter case (with the corresponding modifications of Eqs. (18)–(21) will be used for the calculation of the local truncation error and the stencil coefficients for the second stencil equation with j=2; see below.

2.2.6 The final expression for a Taylor series of the local truncation error

Below, we consider the local truncation error for the first stencil equation, Eq. (13) with j=1. The derivations of the local truncation error for the second stencil equation, Eq. (13) with j=2, can be done similarly (see also Sect. 2.2.5). Inserting Eqs. (14) and (15) and Eqs. (16)–(21) with zero body forces $f_{G,x}^* = f_{G,y}^* = f_{G,x}^{**} = f_{G,y}^{**} = 0$ into Eq. (13) we will get the following local truncation error in space e_1 :

$$\begin{split} e_1 &= b_{1,1} u_G^* + b_{1,2} v_G^* + b_{1,3} u_G^{**} + b_{1,4} v_G^{**} \\ &+ h \left(b_{1,5} \frac{\partial u_G^*}{\partial x} + b_{1,6} \frac{\partial v_G^*}{\partial x} + b_{1,7} \frac{\partial u_G^{**}}{\partial x} + b_{1,8} \frac{\partial v_G^{**}}{\partial x} \right. \\ &+ b_{1,9} \frac{\partial u_G^*}{\partial y} + b_{1,10} \frac{\partial v_G^*}{\partial y} \\ &+ b_{1,11} \frac{\partial u_G^{**}}{\partial y} + b_{1,12} \frac{\partial v_G^{**}}{\partial y} \right) \\ &+ h^2 \left(b_{1,13} \frac{\partial^2 u_G^*}{\partial x \partial y} + b_{1,14} \frac{\partial^2 v_G^*}{\partial x \partial y} + b_{1,15} \frac{\partial^2 u_G^*}{\partial x \partial y} \right. \\ &+ b_{1,16} \frac{\partial^2 v_G^*}{\partial x \partial y} + b_{1,17} \frac{\partial^2 u_G^*}{\partial y^2} + b_{1,18} \frac{\partial^2 v_G^*}{\partial y^2} \right. \\ &+ b_{1,19} \frac{\partial^2 u_G^{**}}{\partial y^2} + b_{1,20} \frac{\partial^2 v_G^{**}}{\partial y^2} \right) \\ &+ h^3 \left(b_{1,21} \frac{\partial^3 u_G^*}{\partial x \partial y^2} + \dots + b_{1,28} \frac{\partial^3 v_G^{**}}{\partial y^3} \right) \\ &+ h^4 \left(b_{1,29} \frac{\partial^4 u_G^*}{\partial x \partial y^3} + \dots + b_{1,36} \frac{\partial^4 v_G^{**}}{\partial y^4} \right) \\ &+ h^5 \left(b_{1,37} \frac{\partial^5 u_G^*}{\partial x \partial y^5} + \dots + b_{1,52} \frac{\partial^6 v_G^{**}}{\partial y^5} \right) \\ &+ h^6 \left(b_{1,45} \frac{\partial^6 u_G^*}{\partial x \partial y^5} + \dots + b_{1,52} \frac{\partial^6 v_G^{**}}{\partial y^5} \right) \\ &+ h^8 \left(b_{1,61} \frac{\partial^8 u_G^*}{\partial x \partial y^5} + \dots + b_{1,60} \frac{\partial^7 v_G^{**}}{\partial y^9} \right) \\ &+ h^9 \left(b_{1,69} \frac{\partial^9 u_G^*}{\partial x \partial y^6} + \dots + b_{1,66} \frac{\partial^9 v_G^{**}}{\partial y^9} \right) \\ &+ h^{10} \left(b_{1,77} \frac{\partial^{10} u_G^*}{\partial x \partial y^9} + \dots + b_{1,84} \frac{\partial^{10} v_G^{**}}{\partial y^{10}} \right) \\ &+ h^{11} \left(b_{1,85} \frac{\partial^{11} u_G^*}{\partial x \partial y^{10}} + \dots + b_{1,92} \frac{\partial^G v_{11}^{**}}{\partial y^{11}} \right) \\ &+ h^{12} \left(b_{1,93} \frac{\partial^{12} u_G^*}{\partial x \partial y^{11}} + \dots + b_{1,100} \frac{\partial^G v_{12}^{**}}{\partial y^{12}} \right) + O(h^{13}) \end{aligned}$$

where the coefficients $b_{1,p}$ (p=1,2,...) are expressed in terms of the coefficients $k_{1,i}$, $\bar{k}_{1,i}$ and $q_{1,m}$, $q_{2,m}$, $q_{3,m}$, $q_{4,m}$ (i=1,2,...,25, $m=1,2,...,N_G$) and are given in Appendix 1. Here, we should mention that the expression for the local truncation error e_1 , Eq. (22), includes only the first-order derivatives with respect to x (the higher order



derivatives with respect to x are excluded with the help of Eqs. (16)–(21)).

2.2.7 Homogeneous materials (no interface)

For homogeneous materials, all a_j (j = 1, 2, ..., 25) coefficients are $a_j = 1$ (see Eq. (11) if we consider material *) as well as all $q_{1,j} = q_{2,j} = q_{3,j} = q_{4,j} = 0$ (j = 1, 2, ..., 9) coefficients are zero. In this case, the derivation of the local truncation error is similar to that in the previous section and is given in our paper [38] and Appendix 2. The local truncation error for the first stencil (see our paper [38] for details) is:

$$\begin{split} e_1 = & \frac{5(\lambda + \mu)(54828\lambda^2 + 102343\lambda\mu + 40202\mu^2)}{9072(1364946\lambda^3 + 23192997\lambda^2\mu + 44409365e\mu^2 + 21238414\mu^3)} \\ & \frac{\partial^{12}u_{A,B}}{\partial y^{12}}h^{12} + O(h^{13}), \end{split} \tag{23}$$

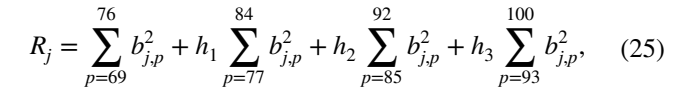
i.e., the order of the local truncation error cannot exceed 12 for any 25-point uniform stencils independent of the method used for their derivation (the finite element method, the finite volume method, the finite difference method, or any other method). The 12-th order of the local truncation error corresponds to the optimal 10-th order of accuracy for the global numerical solution (e.g., see our paper [38]). For the elasticity equations, the accuracy of the new approach with 25-point uniform stencils significantly exceeds the accuracy of conventional high-order finite elements with much wider stencils; see the numerical results below.

2.2.8 25-point stencils for heterogeneous materials with an irregular interface

The formulas presented below can be used for the first j=1 and second j=2 stencils (they should be separately considered for j=1 and j=2). The analytical (with 'Mathematica') and numerical calculations for straight and curvilinear interfaces show that the first 84 coefficients $b_{j,p}$ in Eq. (22) up to the 10-th order with respect to h can be zero. However, some of the coefficients $b_{j,p}$ ($p=69,70,\ldots$) starting from order 9 in Eq. (22) can be linearly dependent. Therefore, in order to minimize the order of the local truncation error e_1 in Eq. (22), we will zero the first 68 coefficients $b_{j,p}$ in Eq. (22) up to the 8-th order with respect to h; i.e.,

$$b_{j,p} = 0, \quad p = 1, 2, \dots, 68.$$
 (24)

Then, to have a sufficient number of equations for the calculation of the 86 stencil coefficients of each stencil including $k_{j,i}$, $\bar{k}_{j,i}$ ($i=1,2,\ldots,25$) and $q_{1,m}$, $q_{2,m}$, $q_{3,m}$, $q_{4,m}$ ($m=1,2,\ldots,9$), we use the least square method for the minimization of coefficients $b_{j,p}$ related to 9-th, 10-th, 11-th and 12-th orders of the local truncation error with the following residual R_i :



where h_1 , h_2 and h_3 are the weighting factors to be selected (e.g., the numerical experiments show that $h_1 = 1/5$, $h_2 = h_1/5$, $h_3 = h_2/5$ yield accurate results and provide the 11-th order of the local truncation error). To minimize the residual R_j with the constraints given by Eq. (24), we can form a new residual \bar{R}_j with the Lagrange multipliers λ_l :

$$\bar{R}_{j} = \sum_{l=1}^{68} \lambda_{l} b_{j,l} + \sum_{p=69}^{76} b_{j,p}^{2} + h_{1} \sum_{p=77}^{84} b_{j,p}^{2} + h_{2} \sum_{p=85}^{92} b_{j,p}^{2} + h_{3} \sum_{p=93}^{100} b_{j,p}^{2}.$$
(26)

The residual \bar{R}_j is a quadratic function of the stencil coefficients $k_{j,i}$, $\bar{k}_{j,i}$ ($i=1,2,\ldots,25$) and $q_{1,m}$, $q_{2,m},q_{3,m}$, $q_{4,m}$ ($m=1,2,\ldots,9$) and a linear function of the Lagrange multipliers λ_l ; i.e., $\bar{R}_j = \bar{R}_j(k_{j,i},\bar{k}_{j,i},q_{1,m},q_{2,m},q_{3,m},q_{4,m},\lambda_l)$. In order to minimize the residual $\bar{R}_j = \bar{R}_j(k_{j,i},\bar{k}_{j,i},q_{1,m},q_{2,m},q_{3,m},q_{4,m},\lambda_l)$, the following equations based on the least square method for the residual \bar{R}_i can be written down:

$$\frac{\partial \bar{R}_{j}}{\partial k_{j,i}} = 0, \quad \frac{\partial \bar{R}_{j}}{\partial \bar{k}_{j,i}} = 0, \quad \frac{\partial \bar{R}_{j}}{\partial q_{1,m}} = 0,$$

$$\frac{\partial \bar{R}_{j}}{\partial q_{2,m}} = 0, \quad \frac{\partial \bar{R}_{j}}{\partial q_{3,m}} = 0, \quad \frac{\partial \bar{R}_{j}}{\partial q_{4,m}} = 0, \quad \frac{\partial \bar{R}_{j}}{\partial \lambda_{l}} = 0,$$

$$i = 1, 2, \dots, 25, \quad m = 1, 2, \dots, 9, \quad l = 1, 2, \dots, 68,$$
(27)

where the equations $\frac{\partial \bar{R_1}}{\partial k_{1,13}} = \frac{\partial \bar{R_1}}{\partial \bar{k}_{1,13}} = 0$ should be replaced by $k_{1,13}=1$ and $\bar{k}_{1,13}=0$ for the first stencil with j=1 (the equations $\frac{\partial \bar{R}_2}{\partial k_{2,13}}=\frac{\partial \bar{R}_2}{\partial \bar{k}_{2,13}}=0$ should be replaced by $k_{2,13}=0$ and $\bar{k}_{2,13} = 1$ for the second stencil with j = 2); see Sect. 2.2.3. Equation (27) forms a system of 154 linear algebraic equations with respect to 154 unknown coefficients k_{ij} , $\bar{k}_{i,i}$ (i = 1, 2, ..., 25) and $q_{1,m}, q_{2,m}, q_{3,m}, q_{4,m}$ (m = 1, 2, ..., 9) as well as the Lagrange multipliers λ_l (l = 1, 2, ..., 68). Solving these linear algebraic equations numerically, we can find the coefficients $k_{i,i}$, $\bar{k}_{i,i}$ (i = 1, 2, ..., 25) for the 25-point uniform stencils as well as $q_{1,m}, q_{2,m}, q_{3,m}, q_{4,m} (m = 1, 2, ..., 5)$. As can be seen, the presented procedure provides the 11-th order of the local truncation error for the 25-point uniform stencils with the general geometry of the interface. The 25-point uniform stencils of OLTEM for homogeneous materials (without interface) provide the 12-th order of the local truncation error for rectangular meshes; see Eq. (23). This leads to the 10-th order of accuracy of global solutions; see the numerical examples below.



To estimate the computational costs for the solution of 154 linear algebraic equations formed by Eq. (27) for the 25-point stencils, we solved 10³ such systems with the general MATLAB solver 'pinv' on a desktop computer (Processor: Intel(R) Core(TM) i7-10700 CPU @ 2.90 GHz). the computation 'wall' time was T = 57.55s for 10^3 systems or the average time for one system was 0.05755s for the 25-point stencils. Because the coefficients $k_{i,i}$, $\bar{k}_{i,i}$ are independently calculated for different grid points, the computation time of their calculation for different grid points can be significantly reduced on modern parallel computers. For 2-D problems with 1-D interfaces, the number of heterogeneous stencils (the stencils cut by the interface) is proportional to $\frac{1}{2}$ at mesh refinement while the numbers of the internal grid points and the global degrees of freedom (the displacements at the internal grid points) for 2-D domains are proportional to $\frac{1}{12}$. This means that for large global systems of discrete equations at small h, the computation time for the calculation of the coefficients $k_{i,i}$, $\bar{k}_{i,i}$ is very small compared to that for the solution of the global system of discrete equations. We should mention that the coefficients $q_{1,m}$, $q_{2,m}$, $q_{3,m}$, $q_{4,m}$ calculated from the local system of equations, Eq. (27), are only used for the calculation of non-zero right-hand side vector (see Eq. (29) below) and do not introduce additional unknowns to the global system of discrete equations (see Eq. (11)) while the Lagrange multipliers λ_i in the local system of equations, Eq. (27), are not used in the global system of discrete equations at all.

Remark 2 It is interesting to mention that the stencil coefficients can be also derived by using the central grid point with the coordinates x_{13} and y_{13} in Eqs. (14)–(22) instead of the interface point with the coordinates x_G and y_G .

The global system of discrete equations includes the 25-point stencils for homogeneous materials without interfaces and the 25-point stencils for heterogeneous materials with interfaces between different materials (see Fig. 1) for all internal grid points located inside the domain. OLTEM does not use unknowns at the interfaces and the global system of discrete equations has the same unknowns (the displacements u and v at the internal grid points of Cartesian meshes; see Eq. (11)) for homogeneous and heterogeneous materials. OLTEM provides the same structures of the global matrices for homogeneous and heterogeneous materials, the difference is only in the values of the stencil coefficients $k_{j,i}$, $\bar{k}_{j,i}$ of the global matrices.

2.3 Non-zero body forces $f_x^l \neq 0$ and $f_y^l \neq 0$ in Eq. (1)

The inclusion of non-zero body forces $f_x^l \neq 0$ and $f_y^l \neq 0$ in the partial differential equations, Eq. (1), leads to the non-zero terms $\bar{f}_{j,13}$ in the stencil equations, Eq. (11) (similar

to Eq. (6)). As we mentioned after Eq. (1), the body forces f_x^l and f_y^l can be discontinuous across the interfaces. The expressions for the terms $\bar{f}_{j,13}$ can be calculated from the procedure used for the derivation of the local truncation error in the case of zero body forces as follows (here, we will show the derivation of the term $\bar{f}_{1,13}$ for the first stencil equation, Eq. (11), with j=1). The insertion of Eqs. (14) and (15) and Eqs. (16)–(21) with non-zero body forces into Eq. (13) yields the following local truncation error in space e_1^f :

$$e_{1}^{f} = e_{1} - \left[\bar{f}_{1,13} + \mathbf{h}^{2} \left(\frac{1}{2(\lambda_{*} + 2\mu_{*})} p_{1} f_{G,x}^{*} + (\dots) f_{G,y}^{*} + (\dots) f_{G,y}^{*} + (\dots) f_{G,y}^{**} + (\dots) f_{G,y}^{**} + \mathbf{h}^{3} \dots\right],$$
(28)

where e_1 is the local truncation error in space given by Eq. (22) for zero body forces, $\tilde{f}_{G,x}^*$, $\tilde{f}_{G,x}^*$, $\tilde{f}_{G,y}^*$ and $\tilde{f}_{G,y}^{**}$ designate the body forces f_x^* , f_x^{**} , f_y^* and f_y^{**} calculated at the central interface point with the coordinates $x = x_G$ and $y = y_G$, the expression for p_1 is given in Appendix 3. Equating to zero the expression in the square brackets in the right-hand side of Eq. (28), we will get the expression for $\bar{f}_{1,13}$:

$$\bar{f}_{1,13} = -\mathbf{h}^2 \left(\frac{1}{2(\lambda_* + 2\mu_*)} p_1 f_{G,x}^* + (\dots) f_{G,y}^* + (\dots) f_{G,y}^* + (\dots) f_{G,x}^{**} + (\dots) f_{G,y}^{**} \right) - \mathbf{h}^3 \dots,$$
(29)

as well as we will get the same local truncation errors $e_1^f = e_1$ for zero and non-zero body forces (see the attached file 'RHS.nb' for the detailed expression of $\bar{f}_{1,13}$). This means that the coefficients $k_{j,i}$, $\bar{k}_{j,i}$ ($i=1,2,\ldots,25,\ j=1,2$) of the stencil equations are first calculated for zero body forces $f_x^* = f_x^{**} = f_y^* = f_y^{**} = 0$ as described in Sect. 2.2. Then, the nonzero term $\bar{f}_{1,13}$ given by Eq. (29) is used in the stencil equation, Eq. (11) for nonzero body forces.

The derivation of the term $\bar{f}_{2,13}$ for the second stencil equation, Eq. (11), with j=2 can be done similar to that for $\bar{f}_{1,13}$. To preserve symmetry in the derivations for the first and second stencils with respect to the x and y coordinates, for the second stencil with j=2, Eqs. (16) and (17) (with the corresponding modifications of Eqs. (18)–(21)) should express the second y derivatives in terms of the second x derivatives and the second mixed derivatives (see Sect. 2.2.5).

3 New post-processing procedure for stress calculations

Recently, in our paper [44], we have proposed a new postprocessing procedure for the calculation of the spatial derivatives of numerical solutions for the scalar Poisson equation.



It is based on OLTEM with the compact stencils corresponding to linear finite elements. Here, we will extend it to a system of the elasticity equations and to more complicated stencils corresponding to quadratic finite elements. For stress calculations in the 2-D case, we first determine the spatial derivatives $\frac{\partial u^{\text{num}}}{\partial x}$, $\frac{\partial u^{\text{num}}}{\partial y}$, $\frac{\partial v^{\text{num}}}{\partial x}$, $\frac{\partial v^{\text{num}}}{\partial y}$ of the displacements and then calculate the stresses using Hooke's law. Because the calculations of these four derivatives $\frac{\partial u^{\text{num}}}{\partial x}$, $\frac{\partial u^{\text{num}}}{\partial y}$, $\frac{\partial v^{\text{num}}}{\partial y}$, are similar here we show the procedure for the calculation of the spatial derivative $\frac{\partial u^{\text{num}}}{\partial x}$.

The compact 25-point stencils for the calculation of $\frac{\partial u^{\text{num}}}{\partial x}$

The compact 25-point stencils for the calculation of $\frac{\partial u^{\text{min}}}{\partial x}$ at the central stencil point with the coordinates x_{13} and y_{13} (see Fig. 1) can be selected similar to Eq. (11) as follows:

$$-\left[a_{13}\frac{\partial u_{13}^{*,\text{num}}}{\partial x} + (1 - a_{13})\frac{\partial u_{13}^{**,\text{num}}}{\partial x}\right]h + \sum_{p=1}^{25} k_p [a_p u_p^{*,\text{num}} + (1 - a_p)u_p^{**,\text{num}}] + \sum_{p=1}^{25} \bar{k}_p [a_p v_p^{*,\text{num}} + (1 - a_p)v_p^{**,\text{num}}] = \bar{f},$$
(30)

where $\bar{f}=0$ in the case of zero body forces $f_x^l=f_y^l=0$ in Eq. (1), the unknown coefficients k_p and \bar{k}_p ($p=1,2,\ldots,25$) are to be determined from the minimization of the local truncation error, the coefficient $a_{13}=1$ if the central stencil point belongs to material * and $a_{13}=0$ if the central stencil point belongs to material **. It is interesting to note that in contrast to known post-processing procedures for the elasticity equations (e.g., used with finite elements), the calculation of $\frac{\partial u^{\text{num}}}{\partial x}$ includes not only the numerical solution for the displacement u but also for the displacement v; see Eq. (30).

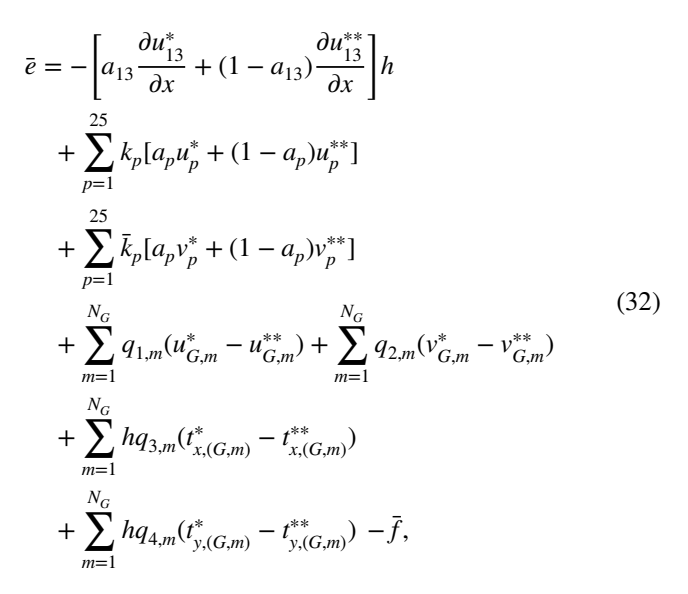
The local truncation error \bar{e} for Eq. (30) can be obtained by the replacement of the numerical solution $u_p^{*,\mathrm{num}}, u_p^{**,\mathrm{num}}, v_p^{**,\mathrm{num}}$ in Eq. (30) by the exact solution $u_p^*, u_p^{**}, v_p^{**}, v_p^{**}$:

$$\bar{e} = -\left[a_{13}\frac{\partial u_{13}^*}{\partial x} + (1 - a_{13})\frac{\partial u_{13}^{***}}{\partial x}\right]h$$

$$+ \sum_{p=1}^{25} k_p [a_p u_p^* + (1 - a_p) u_p^{***}]$$

$$+ \sum_{p=1}^{25} \bar{k}_p [a_p v_p^* + (1 - a_p) v_p^{***}] - \bar{f}.$$
(31)

Similar to Eq. (13) in Sect. 2, we add the interface conditions for the exact solution at the same small number N_G of the interface points into the expression for the local truncation error in Eq. (31) as follows:



where

$$t_{x,(G,m)}^{*(**)} = n_{x,m} \left[(\lambda_{*(**)} + 2\mu_{*(**)}) \frac{\partial u_{G,m}^{*(**)}}{\partial x} + \lambda_{*(**)} \frac{\partial v_{G,m}^{*(**)}}{\partial y} \right]$$

$$+ n_{y,m} \mu_{*(**)} \left(\frac{\partial u_{G,m}^{*(**)}}{\partial y} + \frac{\partial v_{G,m}^{*(**)}}{\partial x} \right),$$

$$t_{y,(G,m)}^{*(**)} = n_{y,m} \left[(\lambda_{*(**)} + 2\mu_{*(**)}) \frac{\partial v_{G,m}^{*(**)}}{\partial y} + \lambda_{*(**)} \frac{\partial u_{G,m}^{*(**)}}{\partial x} \right]$$

$$+ n_{x,m} \mu_{*(**)} \left(\frac{\partial u_{G,m}^{*(**)}}{\partial y} + \frac{\partial v_{G,m}^{*(**)}}{\partial x} \right),$$

$$(33)$$

see the corresponding explanations in Sect. 2.2. Similar to Sect. 2, using the least square method we can form the local system of equations for the calculation of the stencil coefficients k_p and \bar{k}_p ($p=1,2,\ldots,25$) that provide the same order of the local truncation error as that in Sect. 2. The term \bar{f} is calculated similar to the term $\bar{f}_{1,13}$ in Sect. 2.3 with the help of Eq. (29). Finally, the spatial derivative $\frac{\partial u^{\text{num}}}{\partial x}$ is calculated from Eq. (30) for each internal grid point as follows:

$$\frac{\partial u_{13}^{*,\text{num}}}{\partial x} = \frac{1}{h} \left[\sum_{p=1}^{25} k_p [a_p u_p^{*,num} + (1 - a_p) u_p^{**,num}] + \sum_{p=1}^{25} \bar{k}_p [a_p v_p^{*,num} + (1 - a_p) v_p^{**,num}] - \bar{f} \right],$$
(34)

if the central stencil point belongs to material $*(a_{13} = 1)$ and



$$\frac{\partial u_{13}^{**,\text{num}}}{\partial x} = \frac{1}{h} \left[\sum_{p=1}^{25} k_p [a_p u_p^{*,\text{num}} + (1 - a_p) u_p^{**,\text{num}}] + \sum_{p=1}^{25} \bar{k}_p [a_p v_p^{*,\text{num}} + (1 - a_p) v_p^{**,\text{num}}]] - \bar{f} \right],$$
(35)

if the central stencil point belongs to material ** ($a_{13}=0$); see also the detailed description of the post-processing procedure for the Poisson equation in our paper [44]. For the calculations of the spatial derivatives $\frac{\partial u^{\text{num}}}{\partial x}$, $\frac{\partial v^{\text{num}}}{\partial x}$, $\frac{\partial v^{\text{num}}}{\partial y}$, the derivative $\frac{\partial u^{\text{num}}}{\partial x}$ in the first two terms of Eq. (30) should be replaced by the corresponding derivative $\frac{\partial u^{\text{num}}}{\partial y}$, $\frac{\partial v^{\text{num}}}{\partial x}$ or $\frac{\partial v^{\text{num}}}{\partial y}$. The proposed post-processing procedure provides a very high order of accuracy for the stresses (see below the numerical results in Sect. 4.2). It is based on OLTEM with the same 25-point compact stencils as those used in basic computations and it uses the entire system of the elasticity PDEs for post-processing.

4 Numerical examples

In this section, the computational efficiency of OLTEM developed for the 2-D time-independent elasticity interface problems will be demonstrated and compared with conventional linear and high-order (up to the fifth order) finite elements. The commercial finite element software 'COMSOL' is used for the finite element simulations. Similar to FEM terminology, a grid point of a Cartesian mesh will be called a node. To compare the accuracy of the numerical results obtained by OLTEM and by FEM, the relative error e_s^i at the jth node and the maximum relative error e_s^{max} for the variable s are defined as:

$$e_s^j = \frac{|s_j^{\text{num}} - s_j^{\text{exact}}|}{s_{\text{max}}^{\text{exact}}}, \quad e_s^{\text{max}} = \max_j e_s^j, \quad j = 1, 2, \dots, N.$$
(36)

In Eq. (36), the superscripts 'num' and 'exact' correspond to the numerical and exact solutions, N is the total number of nodes used in calculations, $s_{\text{max}}^{\text{exact}}$ is the maximum absolute

value of the exact solution for the variable s over the entire domain. We also use the relative error $e_s^{L^2}$ in the L^2 norm for finite elements (e.g., see [45]) and the relative error $e_s^{l^2}$ in the l^2 norm (e.g., see [46]) for OLTEM:

$$e_s^{l^2} = \frac{\|s^{\text{exact}} - s^{\text{num}}\|_{l^2}}{\|s^{\text{exact}}\|_{l^2}},$$
(37)

where $\|s^{\text{exact}} - s^{\text{num}}\|_{\ell^2} = \{ dx dy \sum_{i=0}^{N_x} \sum_{j=0}^{N_y} [s^{\text{exact}}(x_i, y_j) - s^{\text{num}}(x_i, y_j)]^2 \}^{\frac{1}{2}}$. N_x and

 N_y are the numbers of Cartesian grid points along the x- and y-axes, x_i and y_j are the coordinates of Cartesian grid points. The displacements u and v as well as the normal s_x , s_y and shear s_{xy} stresses are considered as variable s in Eqs. (36) and (37).

4.1 A square plate with a circular interface

4.1.1 The problem formulation and the exact solution

Let us consider a square plate ABCD with dimensions 2×2 ; see Fig. 2. A circular interface with radius $r_0 = \pi/8$ centered at the origin O(0,0) divides the domain Ω into two subdomains: the circular subdomain $\Omega_{\rm II}$ and the remaining subdomain $\Omega_{\rm II}$. For the circular interface, the components of the unit normal used in the interface conditions equal $n_x = \frac{x}{r_0}$ and $n_y = \frac{y}{r_0}$ for any interface point with the coordinate (x, y). Using the method of manufactured solutions, the following exact solution (e.g., see [47]) is selected:

$$\begin{cases} u_{\rm I}(x,y) = \frac{(\sqrt{r^2+1})^{\alpha}}{\lambda_{\rm I}}, \\ v_{\rm I}(x,y) = \frac{(\sqrt{r^2+1})^{\beta}}{\lambda_{\rm I}}, \end{cases} & \text{in } \Omega_{\rm I} \\ u_{\rm II}(x,y) = \frac{(\sqrt{r^2+1})^{\alpha}}{\lambda_{\rm II}} + (\frac{1}{\lambda_{\rm I}} - \frac{1}{\lambda_{\rm II}}) \left(\sqrt{r_0^2+1}\right)^{\alpha}, \\ v_{\rm II}(x,y) = \frac{(\sqrt{r^2+1})^{\beta}}{\lambda_{\rm II}} + (\frac{1}{\lambda_{\rm I}} - \frac{1}{\lambda_{\rm II}}) \left(\sqrt{r_0^2+1}\right)^{\beta}, \end{cases} & \text{in } \Omega_{\rm II} \end{cases}$$

$$(38)$$

where $\alpha = -7$, $\beta = -10$ and $r = \sqrt{x^2 + y^2}$. The body forces can be calculated by the substitution of the exact solution into the elasticity equations and are given below:

$$\begin{cases} f_x^{\rm I}(x,y) = -\frac{xy(\sqrt{r^2+1})^\beta(-2+\beta)\beta(\lambda_{\rm I}+\mu_{\rm I})+(\sqrt{r^2+1})^\alpha\alpha((1+y^2+x^2(-1+\alpha))\lambda_{\rm I}+(3+y^2(1+\alpha)+x^2(-1+2\alpha))\mu_{\rm I})}{(1+r^2)^2\lambda_{\rm I}}, & \text{in } \Omega_{\rm I} \\ f_y^{\rm I}(x,y) = -\frac{xy(\sqrt{r^2+1})^\alpha(-2+\alpha)\alpha(\lambda_{\rm I}+\mu_{\rm I})+(\sqrt{r^2+1})^\beta\beta((1+x^2+y^2(-1+\beta))\lambda_{\rm I}+(3+x^2(1+\beta)+y^2(-1+2\beta))\mu_{\rm I})}{(1+r^2)^2\lambda_{\rm I}}, & \text{in } \Omega_{\rm I} \end{cases}$$

$$\begin{cases} f_x^{\rm II}(x,y) = -\frac{xy(\sqrt{r^2+1})^\beta(-2+\beta)\beta(\lambda_{\rm II}+\mu_{\rm II})+(\sqrt{r^2+1})^\alpha\alpha((1+y^2+x^2(-1+\alpha))\lambda_{\rm II}+(3+y^2(1+\alpha)+x^2(-1+2\alpha))\mu_{\rm II})}{(1+r^2)^2\lambda_{\rm I}}, & \text{in } \Omega_{\rm II} \end{cases}$$

$$\begin{cases} f_x^{\rm II}(x,y) = -\frac{xy(\sqrt{r^2+1})^\beta(-2+\beta)\beta(\lambda_{\rm II}+\mu_{\rm II})+(\sqrt{r^2+1})^\alpha\alpha((1+y^2+x^2(-1+\alpha))\lambda_{\rm II}+(3+y^2(1+\alpha)+x^2(-1+2\alpha))\mu_{\rm II})}{(1+r^2)^2\lambda_{\rm I}}, & \text{in } \Omega_{\rm II} \end{cases}$$



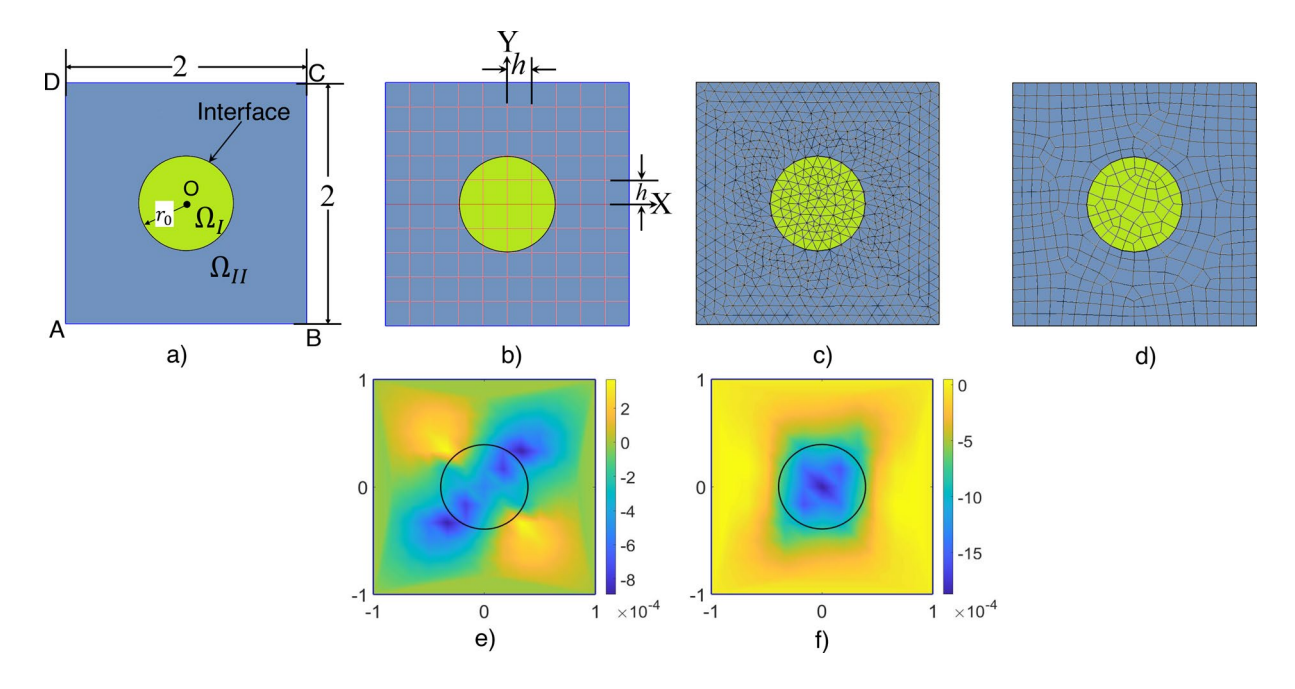


Fig. 2 A square plate *ABCD* with a circular interface centered at O(0,0) with a radius $r_0 = \pi/8$ (a). Examples of a square unfitted Cartesian mesh for OLTEM (b), of conformed triangular (c) and quadri-

lateral (**d**) finite element meshes generated by COMSOL. The distribution of the relative errors e_u (**e**) and e_v (**f**) obtained by OLTEM on a square Cartesian mesh with size h = 1/6

4.1.2 Material parameters

The following elastic Lame's coefficients λ and μ are used for this problem: (1) $\lambda_{\rm I}=10$, $\lambda_{\rm II}=5$, $\mu_{\rm I}=4$, $\mu_{\rm II}=2$ for compressible materials and (2) $\lambda_{\rm I}=\frac{75924000}{20993}$, $\lambda_{\rm II}=\frac{37962000}{20993}$, $\mu_{\rm II}=\frac{38000}{20993}$ for nearly incompressible materials. They correspond to the same Poisson's ratio $v_{\rm I}=v_{\rm II}=\frac{5}{14}=0.357$ and the following Young's moduli $E_{\rm I}=\frac{76}{E_{\rm I}}$, $E_{\rm II}=\frac{38}{7}$ with the contrast for Young's moduli $E_{\rm c}=\frac{E_{\rm I}}{E_{\rm II}}=2$ for compressible materials as well as to the same Poisson's ratio $v_{\rm I}=v_{\rm II}=0.4995$ and the following Young's moduli $E_{\rm I}=\frac{76}{E_{\rm I}}$, $E_{\rm II}=\frac{38}{7}$ with the contrast for Young's moduli $E_{\rm I}=\frac{76}{E_{\rm I}}$, $E_{\rm II}=\frac{38}{7}$ with the contrast for Young's moduli $E_{\rm I}=\frac{76}{E_{\rm I}}=2$ for nearly incompressible materials. The exact solution given by Eq. (38) with the selected material properties meets the interface conditions, Eqs. (3) and (4).

4.1.3 Numerical solutions by OLTEM and FEM

The test problem is solved by OLTEM on square ($b_y = 1$) Cartesian meshes as well as by conventional linear and high-order (up to the fifth order which is the maximum order implemented in COMSOL) finite elements; see Fig. 2b for an example of an unfitted Cartesian mesh used with OLTEM and see Fig. 2c, d for examples of conformed triangular and quadrilateral finite element meshes generated by COMSOL. The Dirichlet boundary conditions are imposed along the edges of the square plate according to the exact solution

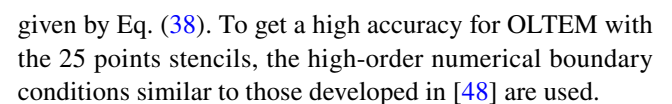
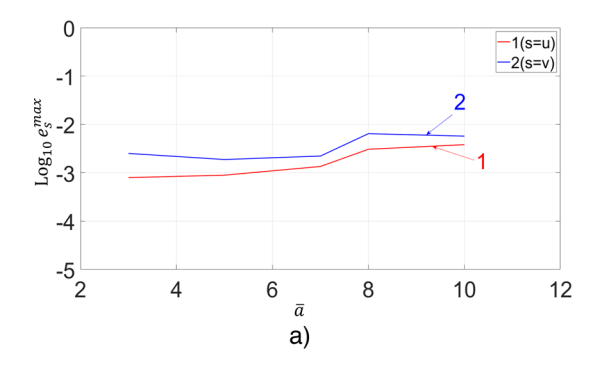


Figure 2e, f shows the distribution of the relative errors e_u (Fig. 2e) and e_v (Fig. 2f) obtained by OLTEM for the compressible materials on a square Cartesian mesh with size h = 1/6. As can be seen from Fig. 2e, f the errors e_u and e_v are very small for this mesh; i.e., OLTEM yields accurate results.

Figures 3 and 4 present the numerical study of the distances $\bar{h}=h/\bar{a}$ between the interface points (Fig. 3) as well as of the weighting coefficients $h_1=\bar{w},\,h_2=h_1\bar{w},\,h_3=h_2\bar{w}$ (Fig. 4) on the accuracy of numerical results for the maximum relative errors $e_u^{\max},\,e_v^{\max}$ (a) and the errors $e_u^{\ell},\,e_v^{\ell}$ in the ℓ^2 norm (b) for the spherical interfaces with the Cartesian mesh of the mesh size h=1/6. Based on the analysis of these figures, we selected $\bar{h}=h/5$ as well as $h_1=1/5,\,h_2=h_1/5,\,h_3=h_2/5$ for all numerical results presented in the paper.

To study the convergence of the numerical results obtained by OLTEM for compressible and nearly incompressible materials, Fig. 5 shows the maximum relative errors e_u^{\max} , e_v^{\max} (a, b) and the errors $e_u^{l^2}$, $e_v^{l^2}$ in the l^2 norm (c, d) as a function of the mesh size h in the logarithmic scale. The slopes of the curves in Fig. 5 correspond the order of convergence. As can be seen from Fig. 5, the order of convergence of OLTEM is close to 10 for compressible (curve 1) and nearly incompressible (curve 2) materials (the tenth order of convergence in Fig. 5 is designated by a straight





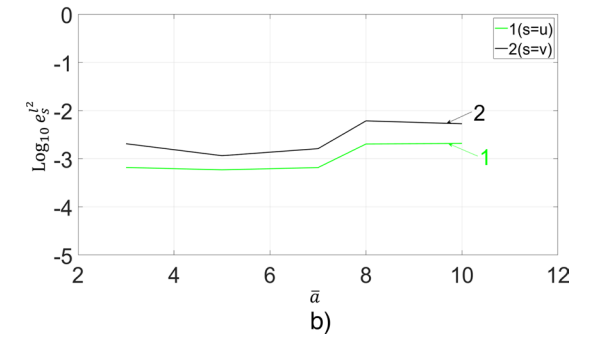
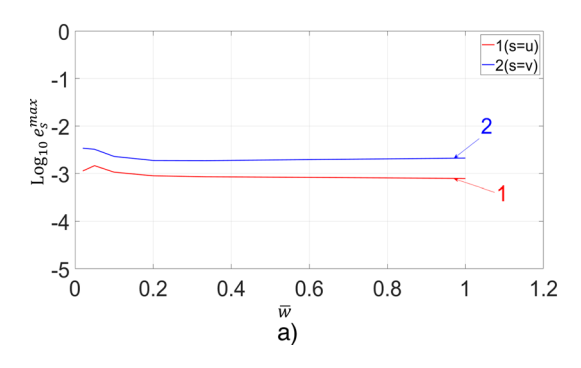


Fig. 3 The maximum relative errors e_u^{\max} (curve 1 in **a**) and e_v^{\max} (curve 2 in **a**) as well as the errors $e_u^{l^2}$ (curve 1 in **b**) and $e_v^{l^2}$ (curve 2 in **b**) in the l^2 norm in the logarithmic scale as a function of the parameter \bar{a} related to the distances $\bar{h} = h/\bar{a}$ between the interface points (see

the corresponding text). The numerical solutions for the test problem with the circular interface are obtained by OLTEM on the square Cartesian mesh of size h = 1/6 for the compressible materials



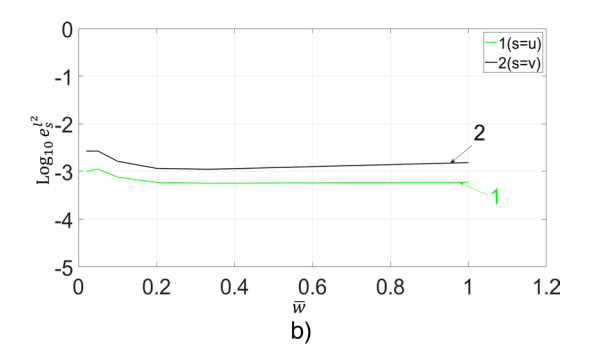


Fig. 4 The maximum relative errors e_u^{max} (curve 1 in **a**) and e_v^{max} (curve 2 in **a**) as well as the errors $e_u^{l^2}$ (curve 1 in **b**) and $e_v^{l^2}$ (curve 2 in **b**) in the l^2 norm in the logarithmic scale as a function of the parameter \bar{w} related to the weighting coefficients $h_1 = \bar{w}$, $h_2 = h_1\bar{w}$, $h_3 = h_2\bar{w}$

(see the corresponding text). The numerical solutions for the test problem with the circular interface are obtained by OLTEM on the square Cartesian mesh of size h = 1/6 for the compressible materials

line 3). This is in agreement of the theoretical results of Sect. 2. We can also mention that OLTEM yields more accurate results for compressible materials compared to those for nearly incompressible materials (see curves 1 and 2) as well as some variations in the slope of curve 2 for nearly incompressible materials can be observed at mesh refinement. Nevertheless, OLTEM provides very accurate results for nearly incompressible materials as well.

To compare the accuracy of the numerical solutions obtained by OLTEM and by finite elements, Figs. 6 and 7 show the maximum relative errors e_u^{\max} , e_u^{\max} (a, b) and the errors $e_u^{L^2}$, $e_v^{L^2}$ in the L^2 norm (c, d) as a function of the number N of degrees of freedom for the compressible (Fig. 6) and nearly incompressible (Fig. 7) materials. As can be seen from Figs. 6 and 7, at the same N the numerical results obtained by OLTEM are much more accurate than those obtained by linear and high-order (up to the 5th order) quadrilateral and triangular finite elements; compare curve 11 with curves 1–10. We should mention that high-order (starting from the third order) finite elements have a much greater width of stencil equations compared to that for OLTEM with

the 25-point stencils. This leads to a significant reduction in computation costs for OLTEM with unfitted meshes compared to finite elements with conformed meshes at the same accuracy.

4.1.4 The accuracy study of OLTEM at small variations of the mesh size

To study the convergence and stability of the numerical results obtained by OLTEM in more detail, curves 1 and 2 in Fig. 8 present the curves 1 in Fig. 5 at small changes of the mesh size h. For this study, we solve the test problem on 1000 Cartesian meshes with the mesh sizes $h_i = h_1 - 0.0001(i-1)$ where $h_1 = 0.19$ and i = 1, 2, ..., 1000. The grid lines of these meshes along the sides AB and AD (see Fig. 2a) are fixed; i.e., there is a gradual change of the position of the circular interface with respect to Cartesian meshes. As can be seen from Fig. 8, the numerical results obtained by OLTEM on these Cartesian meshes converge with the decrease in the grid size h. Small oscillations in Fig. 8 can be explained by the fact that at



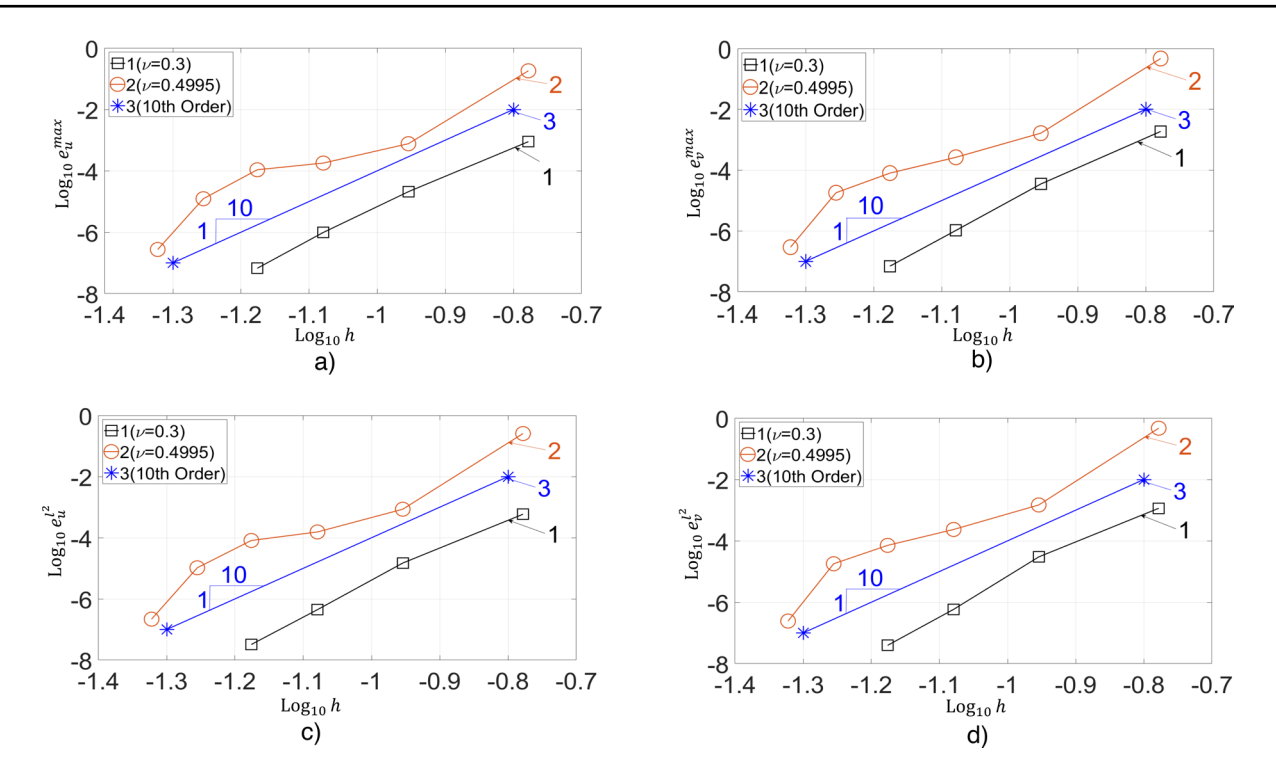


Fig. 5 The maximum relative errors $e_u^{\max}(\mathbf{a})$ and $e_v^{\max}(\mathbf{b})$ as well as the errors $e_u^{l^2}(\mathbf{c})$ and $e_v^{l^2}(\mathbf{d})$ in the l^2 norm as a function of the mesh size h in the logarithmic scale. The numerical solutions for the test problem with the circular interface are obtained by OLTEM on

square Cartesian meshes for compressible (curves 1) and nearly incompressible (curves 2) materials. The reference line 3 designates the 10th order of convergence

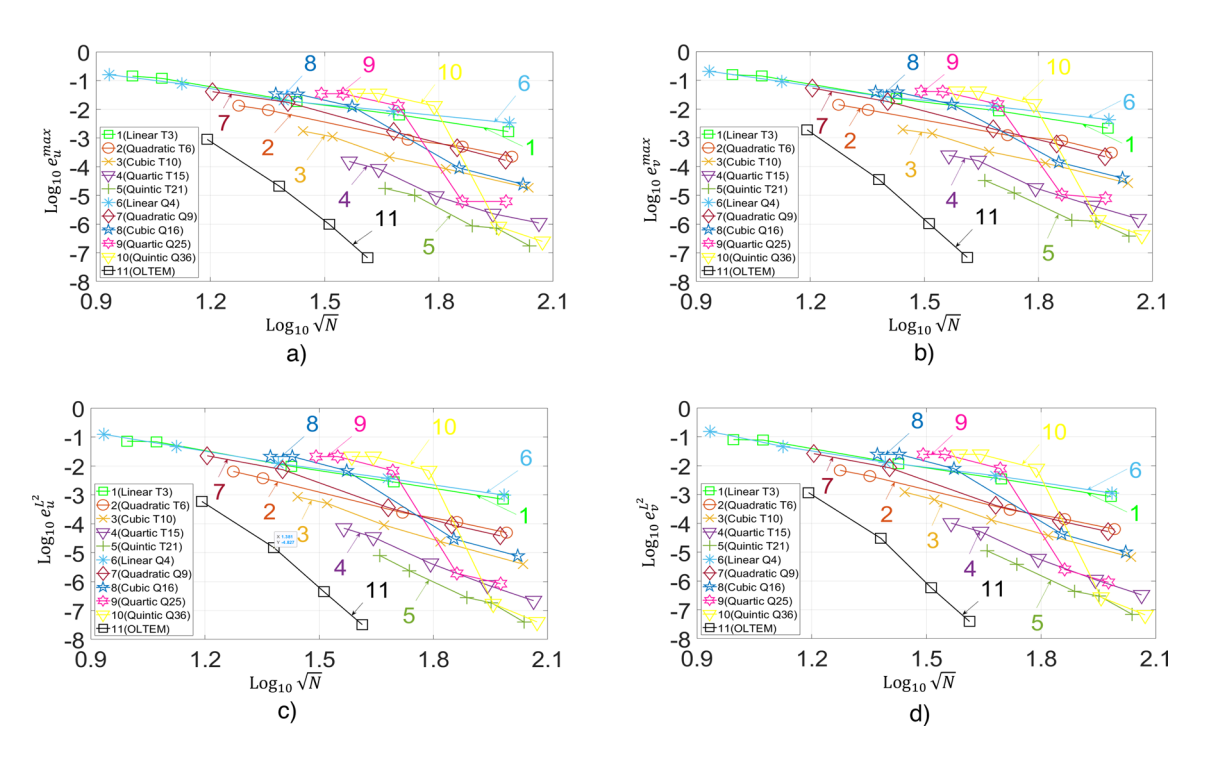


Fig. 6 The maximum relative errors e_u^{\max} (**a**) and e_v^{\max} (**b**) as well as the errors $e_u^{l^2}$ (**c**) and $e_v^{L^2}$ (**d**) in the L^2 norm as a function of the number N of degrees of freedom in the logarithmic scale. The numerical solutions for the plate with the circular interface and compressible

materials are obtained by OLTEM (curve 11) and by conventional triangular (curves 1–5) and quadrilateral (curves 6–10) finite elements. Curves (1, 6), (2, 7), (3, 8), (4, 9), (5, 10) correspond to linear, quadratic, cubic, 4-th order and 5-th order finite elements, respectively



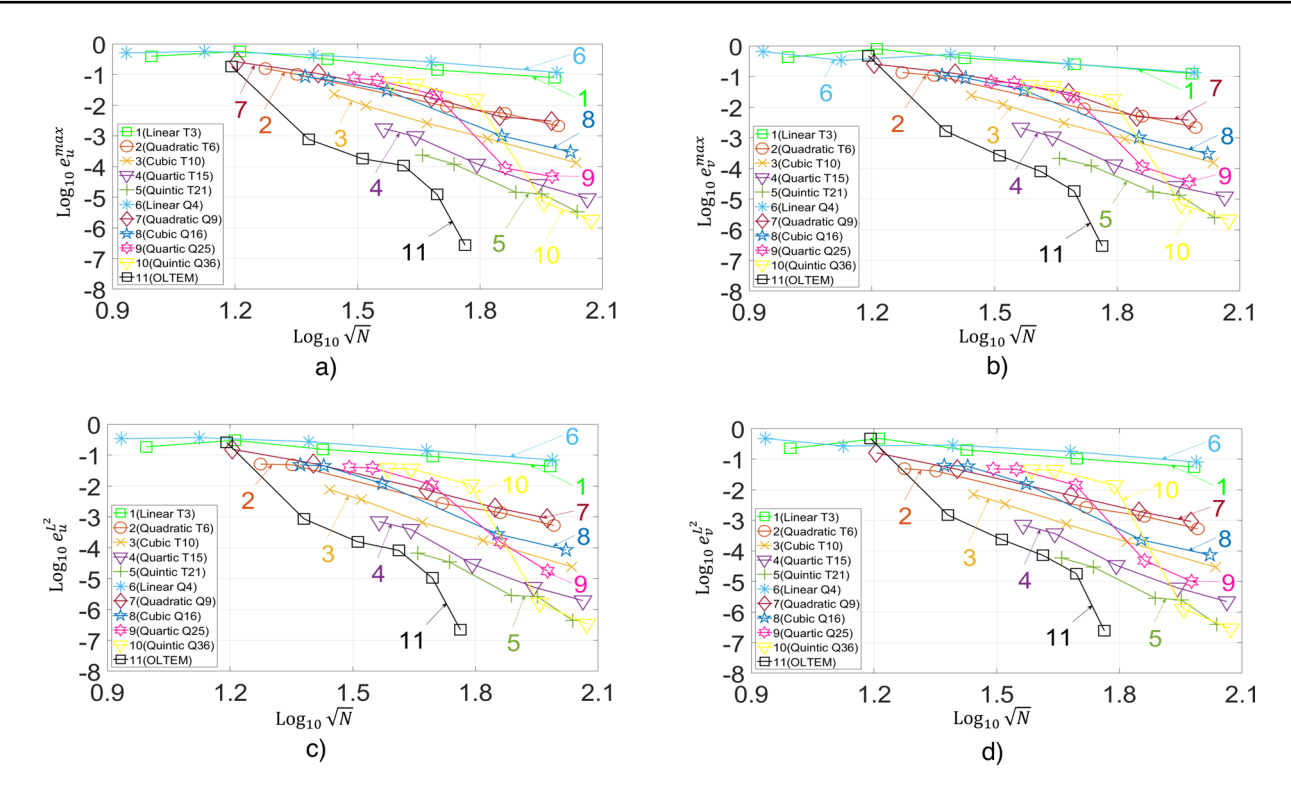


Fig. 7 The maximum relative errors $e_u^{\max}(\mathbf{a})$ and $e_v^{\max}(\mathbf{b})$ as well as the errors $e_u^{L^2}(\mathbf{c})$ and $e_v^{L^2}(\mathbf{d})$ in the L^2 norm as a function of the number N of degrees of freedom in the logarithmic scale. The numerical solutions for the plate with the circular interface and nearly incompressible materials are obtained by OLTEM (curve 11) and by con-

ventional triangular (curves 1-5) and quadrilateral (curves 6-10) finite elements. Curves (1, 6), (2, 7), (3, 8), (4, 9), (5, 10) correspond to linear, quadratic, cubic, 4-th order and 5-th order finite elements, respectively

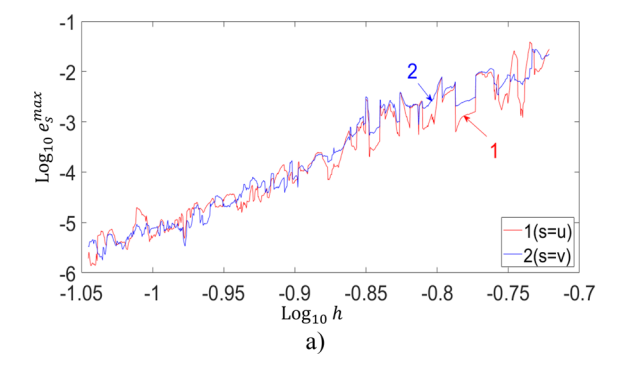
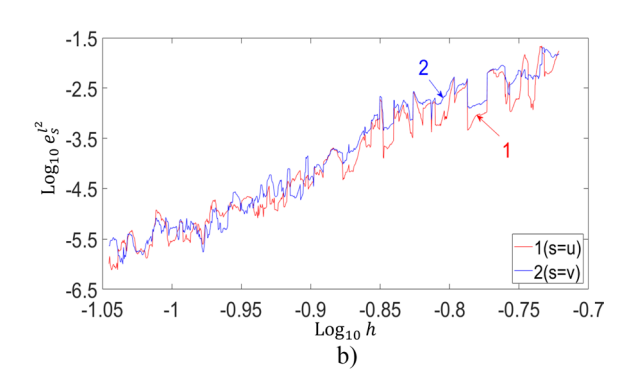


Fig. 8 The maximum relative errors e_u^{\max} (curve 1 in **a**), e_v^{\max} (curve 2 in **a**) and the errors $e_u^{l^2}$ (curve 1 in **b**), $e_v^{l^2}$ (curve 2 in **b**) in the l^2 norm as a function of the mesh size h in the logarithmic scale. The numeri-



cal solutions for the plate with the circular interface for compressible materials are obtained by OLTEM on 1000 square Cartesian meshes

small variations of the mesh size h, there is a discontinuous change in the location of the grid points with respect to the interface (e.g., some grid points that belong to one material for the previous mesh can belong to another material for the next mesh); this leads to the discontinuous change of some stencils equations for the meshes with a small difference in h. It is important to mention that small oscillations in numerical convergence curves are typical for many

numerical techniques at small variations of h. For example, the change in the angles of finite elements at small variations of the element size h also leads to such oscillations in convergence curves for finite element techniques.



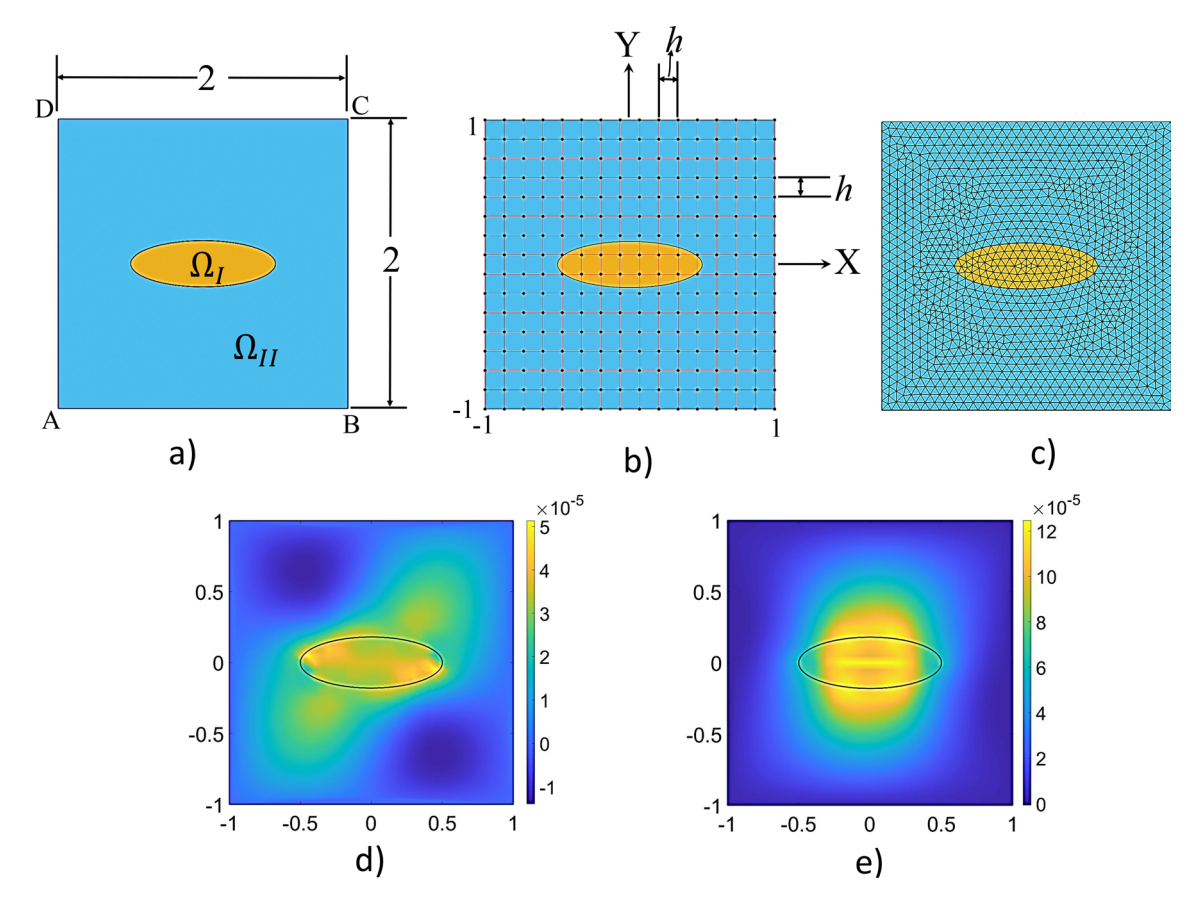


Fig. 9 A square plate ABCD with an elliptical interface centered at point (0, 0) (a). Examples of an unfitted square Cartesian mesh for OLTEM (b), of a conformed triangular finite element mesh (c) gen-

erated by COMSOL. The distribution of the relative errors e_u (d) and e_v (e) obtained by OLTEM on a square Cartesian mesh with size h = 1/20

4.2 A square plate with an elliptical interface

4.2.1 The problem formulation and the exact solution

Here, we consider a problem similar to that the previous Sect. 4.1 but with a more complex elliptical interface given by equation $x^2 + t^2y^2 = 0.5^2$ with t = 2.8; see Fig. 9a. Similar to Sect. 4.1, the exact solution for the problem is also described by Eq. (38) with $\alpha = -7$, $\beta = -10$ and $r = \sqrt{x^2 + t^2y^2}$. The body forces can be calculated by the substitution of the exact solution into the elasticity equations. The compressible materials with the elastic Lame's coefficients that are the same as in Sect. 4.1 are used for this problem. The exact solution given by Eq. (38) with the selected material properties meets the interface conditions, Eqs. (3) and (4). We should mention that similar to FEM, the consideration of composites with one or several inclusions does not change the complexity of the problem for OLTEM but increases the programming efforts for the description of several inclusions. Moreover, a problem with the exact solution can be constructed for one inclusion. This significantly simplifies the analysis of accuracy of numerical results obtained by new methods. The solution of real-world problems with complex geometry requires writing a long code for the geometry description and will be considered in the future.

The test problem is solved by OLTEM on square $(b_y = 1)$ unfitted Cartesian meshes as well as by conventional conformed linear and high-order (up to the fifth order which is the maximum order implemented in COMSOL) triangular finite elements; see Fig. 9b for an example of a Cartesian mesh used with OLTEM and see Fig. 9c for an example of a triangular finite element mesh generated by COM-SOL. Because triangular finite elements yield slightly more accurate results compared to those for quadrilateral finite elements (see the previous Sect. 4.1), here we consider the triangular finite elements only. The Dirichlet boundary conditions are imposed along the edges of the square plate according to the exact solution given by Eq. (38). To get a high accuracy for OLTEM with the 25 points stencils, the high-order numerical boundary conditions similar to those developed in [48] are used.



4.2.2 Numerical solutions by OLTEM and FEM

Figure 9d, e shows the distribution of the relative errors in displacements e_u (Fig. 9d) and e_v (Fig. 9e) obtained by OLTEM on a square Cartesian mesh with size h = 1/20. As can be seen from Fig. 9d, e the errors e_u and e_v are very small for this mesh; i.e., OLTEM yields accurate results.

To study the convergence of the numerical results obtained by OLTEM, Fig. 10 shows the maximum relative errors in displacements e_u^{\max} , e_v^{\max} and the errors in displacements $e_u^{l^2}$, $e_v^{l^2}$ in the l^2 norm as a function of the mesh size h in the logarithmic scale. The slopes of the curves in Fig. 10 correspond the order of convergence. As can be seen from Fig. 10, the order of convergence of OLTEM is close to 10 (the tenth order of convergence in Fig. 10 is designated by a straight line 3). This is in agreement of the theoretical results of Sect. 2.

Based on the new post-processing procedure (see Sect. 3), we calculated the normal s_x , s_y and shear s_{xy} stresses using OLTEM with the compact 25-point stencils (similar to those

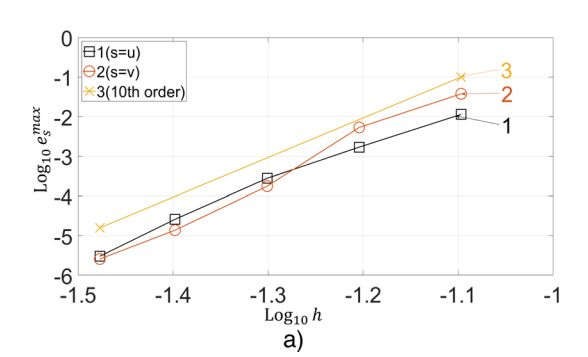


Fig. 10 The maximum relative errors in displacement e_u^{max} (curve 1 in **a**) and e_v^{max} (curve 2 in **a**) as well as the errors in displacement $e_u^{l^2}$ (curve 1 in **b**) and $e_v^{l^2}$ (curve 2 in **b**) in the l^2 norm as a function of the mesh size h in the logarithmic scale. The numerical solutions for the

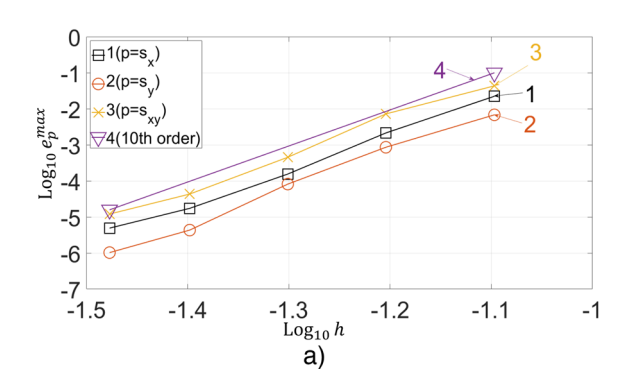
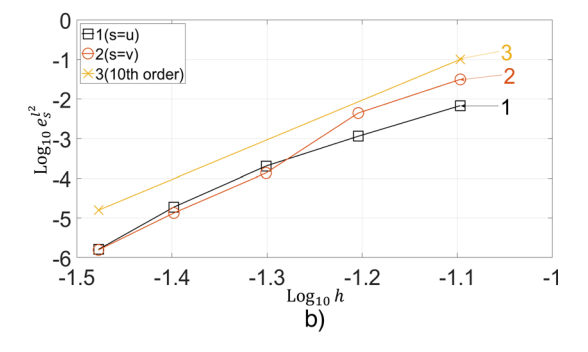


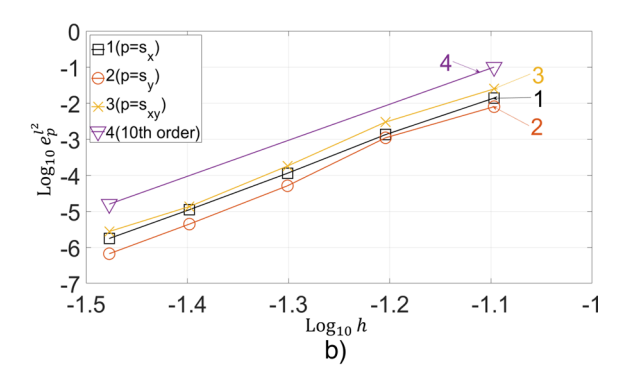
Fig. 11 The maximum relative errors in stresses $e_{s_x}^{\max}$, $e_{s_y}^{\max}$, $e_{s_y}^{\max}$, $e_{s_y}^{\max}$ (curves 1, 2, 3 in **a**) as well as the errors in stresses $e_{s_x}^{\ell^2}$, $e_{s_y}^{\ell^2}$, $e_{s_y}^{\ell^2}$ in the ℓ^2 norm (curves 1, 2, 3 in **b**) as a function of the mesh size h in the loga-

used in basic computations for the displacements). Figure 11 shows the maximum relative errors in stresses $e_{s_x}^{\max}$, $e_{s_y}^{\max}$, $e_{s_x}^{\max}$ and the errors in stresses $e_{s_x}^{l^2}$, $e_{s_y}^{l^2}$, $e_{s_x}^{l^2}$, in the l^2 norm as a function of the mesh size h in the logarithmic scale. As can be seen from Fig. 11, the order of convergence of OLTEM is, in average, close to 10 (the tenth order of convergence in Fig. 11 is designated by a straight line 4).

To compare the accuracy of the numerical solutions obtained by OLTEM and by finite elements, Figs. 12 and 13 show the maximum relative errors in displacements e_u^{\max} , e_v^{\max} and in stresses $e_{s_x}^{\max}$, $e_{s_y}^{\max}$, $e_{s_{xy}}^{\max}$ as well as the errors in displacements $e_u^{L^2}$, $e_v^{L^2}$ and in stresses $e_{s_x}^{L^2}$, $e_{s_y}^{L^2}$, $e_{s_{xy}}^{L^2}$ in the L^2 norm as a function of the number N of degrees of freedom. As can be seen from Figs. 12 and 13, at the same N the displacements and stresses obtained by OLTEM are much more accurate than those obtained by linear and high-order (up to the 5th order) triangular finite elements; compare curve 1 with curves 2–6. We should mention that high-order (starting from the third order) finite elements have a much greater



test problem with the elliptical interface are obtained by OLTEM on unfitted square Cartesian meshes. The reference line 3 designates the 10th order of convergence



rithmic scale. The numerical solutions for the test problem with the elliptical interface are obtained by OLTEM on unfitted square Cartesian meshes. The reference line 4 designates the 10th order of convergence



2.2

2.2

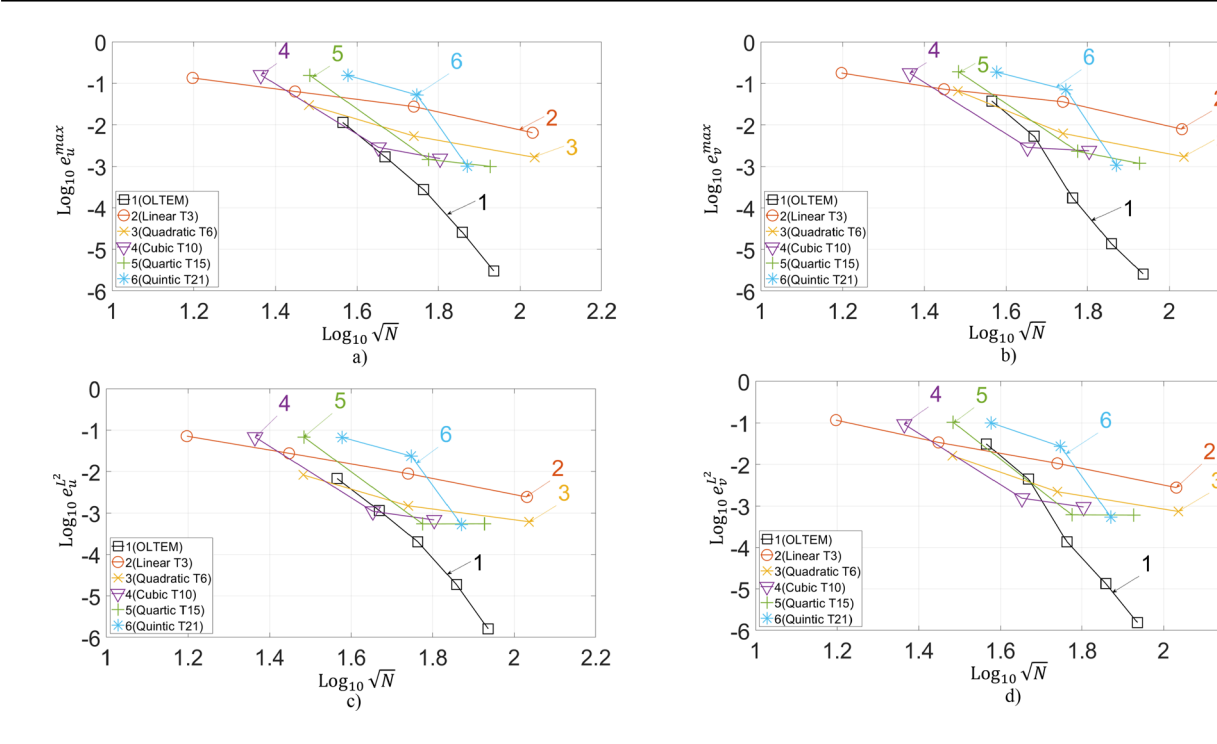


Fig. 12 The maximum relative errors in displacement $e_u^{\max}(\mathbf{a})$ and $e_v^{\max}(\mathbf{b})$ as well as the errors in displacement $e_u^{L^2}(\mathbf{c})$ and $e_v^{L^2}(\mathbf{d})$ in the L^2 norm as a function of the number N of degrees of freedom in the logarithmic scale. The numerical solutions for the plate with the

elliptical interface are obtained by OLTEM (curve 1) and by conventional triangular finite elements (curves 2–6). Curves (2, 3, 4, 5, 6) correspond to linear, quadratic, cubic, 4-th order and 5-th order finite elements, respectively

width of stencil equations compared to that for OLTEM with the 25-point stencils. This leads to a significant reduction in computation costs for OLTEM with unfitted meshes compared to finite elements with conformed meshes at the same accuracy. It is also interesting to note that due to the new post-processing procedure for the stress calculations, the difference in accuracy between OLTEM and FEM is greater for the stresses (see Fig. 13) compared to that for the displacements (see Fig. 12). This is very important for the problems where the accurate calculations of stresses are crucial for accurate predictions (e.g., simulations of crack propagation).

4.2.3 The accuracy study of OLTEM at small variations of the mesh size

To study the convergence and stability of the numerical results with the elliptical interface obtained by OLTEM in more detail, curves 1 and 2 in Fig. 14 present curves 1 and 2 in Fig. 10 at small changes of the mesh size h. For this study, we solve the test problem on 1000 Cartesian meshes with the mesh sizes $h_i = h_1 - 0.00002(i-1)$ where $h_1 = 0.05$ and $i = 1, 2, \ldots, 1000$. The grid lines of these meshes along the sides AB and AD (see Fig. 9a) are fixed; i.e., there is a gradual change of the position of the elliptical interface with

respect to Cartesian meshes. As can be seen from Fig. 14, the numerical results obtained by OLTEM on these Cartesian meshes converge with the decrease in the grid size h (the results are similar to those with the circular interface in Fig. 8 of the previous Sect. 4.1).

It can be concluded that OLTEM with 25-point compact stencils and unfitted Cartesian meshes developed for the 2-D time-independent elasticity interface problems provides the 10th order of accuracy and yields much more accurate results than high order (up to the fifth order) finite elements on conformed meshes and with a greater width of the stencil equations.

5 Concluding remarks

The new numerical approach developed in the paper is the extension of OLTEM for PDEs with constant coefficients (see our papers [35–41]) to a much more general case of 2-D elasticity equations for heterogeneous materials with irregular interfaces. The main idea that allows this extension is the addition of the interface conditions at a small number of the interface points to the expression for the local truncation error. The unknown stencil coefficients can be numerically calculated from a small local system of algebraic equations



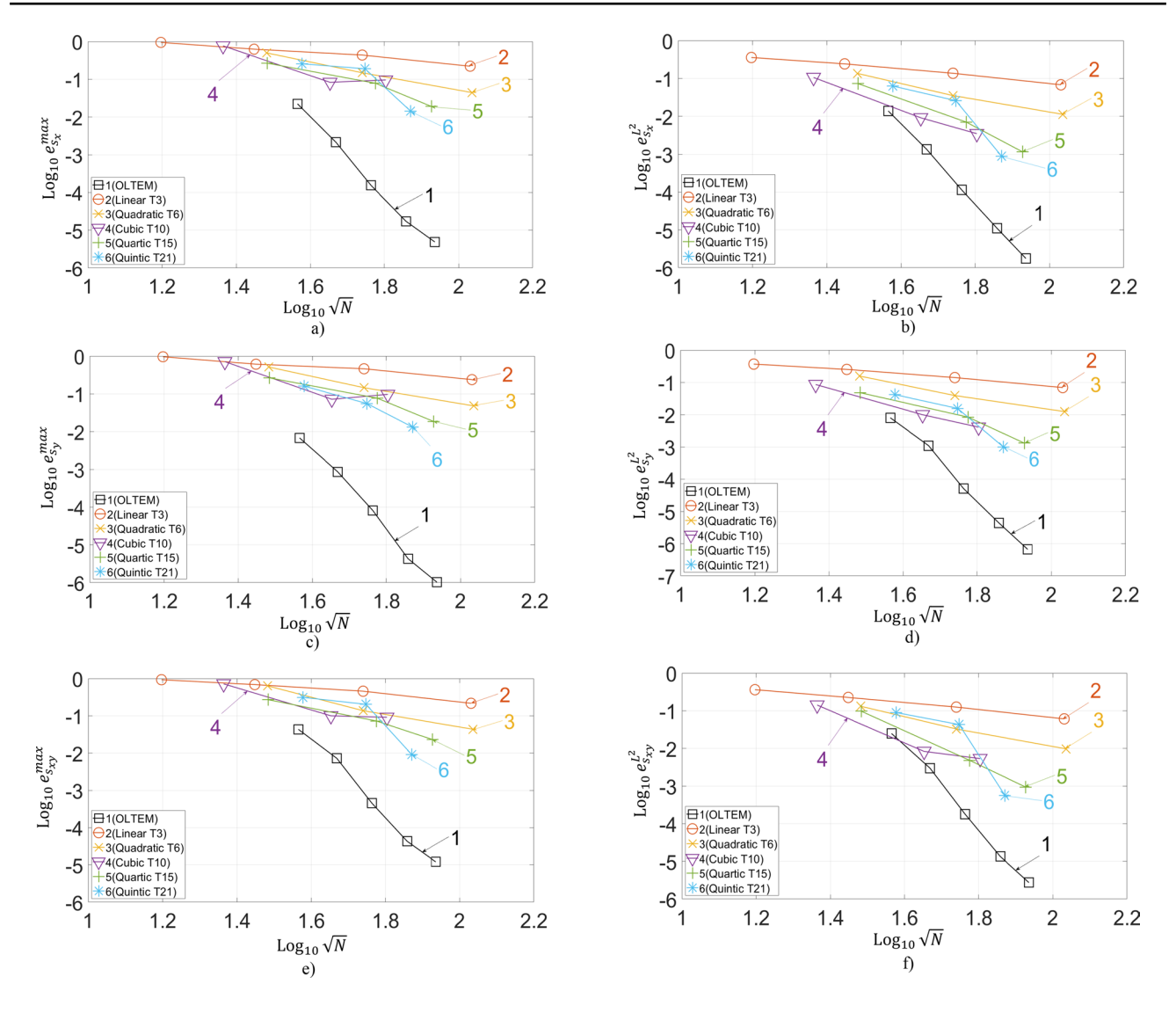


Fig. 13 The maximum relative errors in stresses $e_{s_x}^{\max}(\mathbf{a})$, $e_{s_y}^{\max}(\mathbf{c})$, $e_{s_y}^{\max}(\mathbf{e})$ as well as the errors in stresses $e_{s_x}^{L^2}(\mathbf{b})$, $e_{s_y}^{L^2}(\mathbf{d})$, $e_{s_y}^{L^2}(\mathbf{f})$ in the L^2 norm as a function of the number N of degrees of freedom in the logarithmic scale. The numerical solutions for the plate with the ellipti-

cal interface are obtained by OLTEM (curve 1) and by conventional triangular finite elements (curves 2–6). Curves (2, 3, 4, 5, 6) correspond to linear, quadratic, cubic, 4-th order and 5-th order finite elements, respectively

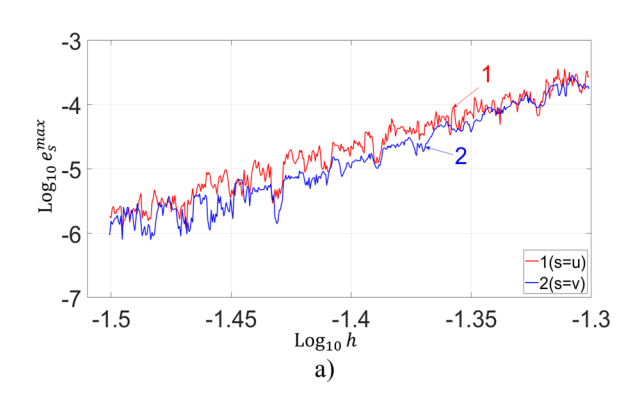
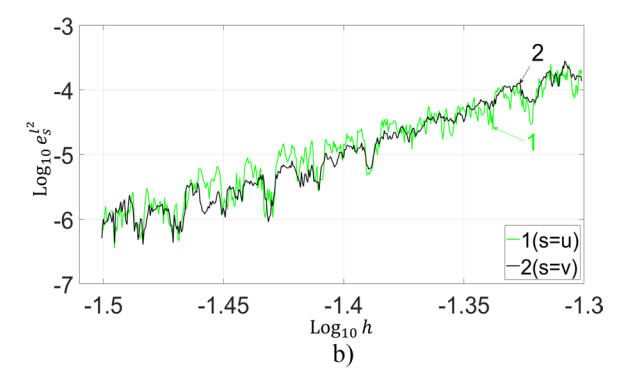


Fig. 14 The maximum relative errors e_u^{\max} (curve 1 in **a**), e_v^{\max} (curve 2 in **a**) and the errors $e_u^{l^2}$ (curve 1 in **b**), $e_v^{l^2}$ (curve 2 in **b**) in the l^2 norm as a function of the mesh size h in the logarithmic scale. The numeri-



cal solutions for the plate with the elliptical interface for compressible materials are obtained by OLTEM on 1000 square Cartesian meshes



for the general geometry of interfaces. This procedure does not change the width of the stencil equation; i.e., the locations of zero and nonzero elements in the global discrete system of equations are the same for homogeneous and heterogeneous materials. The calculation of the unknown stencil coefficients is based on the minimization of the local truncation error of the stencil equations and yields the optimal order of accuracy of the new technique at a given stencil width. The increase in the computational costs for the calculation of the unknown stencil coefficients from the local systems is insignificant compared to the computational costs for the solution of the global discrete system.

The main advantages of the suggested technique can be summarized as follows:

- Many difficulties of the existing numerical techniques for irregular domains (e.g., finite elements, spectral element, isogeometric elements, the finite volume method, and many others) are related to complicated mesh generators and the accuracy of 'bad' elements (e.g., the elements with small angles). In contrast to these techniques, OLTEM is based on simple unfitted Cartesian meshes with a trivial procedure for the formation of the 25-point stencils for 2-D domains with complex irregular interfaces.
- OLTEM has the same width of the stencil equations and the same structure of the global discrete equations for the elasticity equations for homogeneous and heterogeneous materials. There are no unknowns on the interfaces between different materials for the proposed technique; i.e., complex irregular interfaces do not affect the sparse structure of the global system of discrete equations (they affect just the values of the stencils coefficients).
- In contrast to the finite-difference techniques with the stencil coefficients calculated through the approximation of the partial derivatives, the system of partial differential elasticity equations is used for the calculation of the stencil coefficients in OLTEM. This leads to the optimal accuracy of the proposed technique. E.g., the 25-point stencils of OLTEM provide the optimal 10-th order of accuracy that cannot be improved without changing the width of stencil equations. This corresponds to the increase in accuracy by seven orders for OLTEM compared to conventional quadratic finite elements with similar stencils.
- The numerical results for elastic heterogeneous materials with irregular interfaces show that at the same number of degrees of freedom, OLTEM with unfitted meshes is more accurate than high order (up to the fifth order—the

- maximum order implemented in the COMSOL software) finite elements with a much greater stencil width and conformed meshes.
- OLTEM with the 25-point stencils provides very accurate results for nearly incompressible materials (e.g., with Poisson ratio 0.4995).
- A new post-processing procedure for the stress calculations has been developed. Similar to basic computations, it includes OLTEM with the 25-point compact stencils and provides a very high accuracy of the stresses.
- OLTEM does not require time consuming numerical integration for finding the coefficients of the stencil equations; e.g., as for the high-order finite, spectral and isogeometric elements. The stencil coefficients are calculated analytically or numerically (for the general geometry of interfaces) by the solution of small local systems of linear algebraic equations. Numerical experiments show that the solution of these small local systems of algebraic equations is fast. Moreover, these local systems are independent of each other and can be efficiently solved on a parallel computer.

In the future, we plan to extend OLTEM to the 3-D elasticity equations for heterogeneous materials with irregular interfaces. Another direction is the development of OLTEM with adaptive refinement similar to *h*- and *p*-refinement for finite elements (e.g., in our papers [39, 41] we showed that OLTEM can easily combine different stencils). We plan to use quadtrees/octrees meshes that allow a simple refinement strategy with Cartesian meshes. The extension of OLTEM to other PDEs for heterogeneous materials as well as to nonlinear PDEs will be also considered in the future.

Appendix 1: The coefficients $b_{1,p}$ used in Eq. (22) for the first stencils with j=1

The first 10 coefficients $b_{1,p}$ ($p=1,2,\ldots,10$) used in Eq. (22) are presented below in the case of the mesh aspect ratio $b_y=1$. All coefficients $b_{1,p}$ used in these formulas are given in the attached file 'b-coef.nb'. For simplicity of notations, below we use that

$$b_{1,i} = b_i \ (i = 1, 2, \dots, 10), \quad k_{1,i} = k_i, \quad \bar{k}_{1,i} = \bar{k}_i \ (i = 1, 2, \dots, 25),$$

$$q_i = q_{1,i}, \ q_{i+9} = q_{2,i}, \ q_{i+18} = q_{3,i}, \ q_{i+27} = q_{4,i} \ (i = 1, 2, \dots, 9).$$



$$\begin{split} b_1 = & a_1 k_1 + a_{10} k_{10} + a_{11} k_{11} + a_{12} k_{12} \\ & + a_{13} k_{13} + a_{14} k_{14} + a_{15} k_{15} \\ & + a_{16} k_{16} + a_{17} k_{17} + a_{18} k_{18} + a_{19} k_{19} \\ & + a_2 k_2 + a_{20} k_{20} + a_{21} k_{21} \\ & + a_{22} k_{22} + a_{23} k_{23} + a_{24} k_{24} + a_{25} k_{25} + a_{3} k_{3} + a_{4} k_{4} \\ & + a_{5} k_{5} + a_{6} k_{6} + a_{7} k_{7} + a_{8} k_{8} + a_{9} k_{9} \\ & + q_{1} + q_{2} + q_{3} + q_{4} + q_{5} + q_{6} + q_{7} + q_{8} + q_{9} \\ b_{2} = & a_{1} \bar{k}_{1} + a_{10} \bar{k}_{10} + a_{11} \bar{k}_{11} + a_{12} \bar{k}_{12} + a_{13} \bar{k}_{13} + a_{14} \bar{k}_{14} \\ & + a_{15} \bar{k}_{15} + a_{16} \bar{k}_{16} \\ & + a_{17} \bar{k}_{17} + a_{18} \bar{k}_{18} + a_{19} \bar{k}_{19} + a_{2} \bar{k}_{2} + a_{20} \bar{k}_{20} + a_{21} \bar{k}_{21} \\ & + a_{22} \bar{k}_{22} + a_{23} \bar{k}_{23} + a_{24} \bar{k}_{24} + a_{25} \bar{k}_{25} + a_{3} \bar{k}_{3} \\ & + a_{4} \bar{k}_{4} + a_{5} \bar{k}_{5} + a_{6} \bar{k}_{6} + a_{7} \bar{k}_{7} + a_{8} \bar{k}_{8} + a_{9} \bar{k}_{9} \\ & + q_{19} + q_{20} + q_{21} + q_{22} + q_{23} + q_{24} + q_{25} + q_{26} + q_{27} \end{split}$$

$$b_3 = -a_1k_1 - a_{10}k_{10} - a_{11}k_{11} - a_{12}k_{12} - a_{13}k_{13}$$

$$-a_{14}k_{14} - a_{15}k_{15} - a_{16}k_{16}$$

$$-a_{17}k_{17} - a_{18}k_{18} - a_{19}k_{19} - a_2k_2 - a_{20}k_{20} - a_{21}k_{21}$$

$$-a_{22}k_{22} - a_{23}k_{23} - a_{24}k_{24} - a_{25}k_{25} - a_{3}k_{3} - a_{4}k_{4}$$

$$-a_{5}k_5 - a_{6}k_6 - a_{7}k_7 - a_{8}k_8 - a_{9}k_{9}$$

$$+k_1 + k_{10} + k_{11} + k_{12} + k_{13} + k_{14}$$

$$+k_{15} + k_{16} + k_{17} + k_{18} + k_{19}$$

$$+k_2 + k_{20} + k_{21} + k_{22} + k_{23} + k_{24}$$

$$+k_{25} + k_3 + k_4 + k_5 + k_6$$

$$+k_7 + k_8 + k_9 - q_1 - q_2 - q_3 - q_4$$

$$-q_5 - q_6 - q_7 - q_8 - q_9$$

$$\begin{split} b_4 &= -a_1 \bar{k}_1 - a_{10} \bar{k}_{10} - a_{11} \bar{k}_{11} - a_{12} \bar{k}_{12} - a_{13} \bar{k}_{13} \\ &- a_{14} \bar{k}_{14} - a_{15} \bar{k}_{15} - a_{16} \bar{k}_{16} \\ &- a_{17} \bar{k}_{17} - a_{18} \bar{k}_{18} - a_{19} \bar{k}_{19} - a_{2} \bar{k}_{2} - a_{20} \bar{k}_{20} - a_{21} \bar{k}_{21} \\ &- a_{22} \bar{k}_{22} - a_{23} \bar{k}_{23} - a_{24} \bar{k}_{24} - a_{25} \bar{k}_{25} \\ &- a_{3} \bar{k}_{3} - a_{4} \bar{k}_{4} - a_{5} \bar{k}_{5} - a_{6} \bar{k}_{6} - a_{7} \bar{k}_{7} - a_{8} \bar{k}_{8} \\ &- a_{9} \bar{k}_{9} + \bar{k}_{1} + \bar{k}_{10} + \bar{k}_{11} + \bar{k}_{12} + \bar{k}_{13} + \bar{k}_{14} \\ &+ \bar{k}_{15} + \bar{k}_{16} + \bar{k}_{17} + \bar{k}_{18} + \bar{k}_{19} + \bar{k}_{2} \\ &+ \bar{k}_{20} + \bar{k}_{21} + \bar{k}_{22} + \bar{k}_{23} + \bar{k}_{24} + \bar{k}_{25} + \bar{k}_{3} \\ &+ \bar{k}_{4} + \bar{k}_{5} + \bar{k}_{6} + \bar{k}_{7} \\ &+ \bar{k}_{8} + \bar{k}_{9} - q_{19} - q_{20} - q_{21} - q_{22} \\ &- q_{23} - q_{24} - q_{25} - q_{26} - q_{27} \end{split}$$

$$\begin{split} b_5 &= -a_1(\mathrm{d}x_G + 2)k_1 - a_{10}(\mathrm{d}x_G - 2)k_{10} - a_{11}(\mathrm{d}x_G + 2)k_{11} \\ &- a_{12}(\mathrm{d}x_G + 1)k_{12} - a_{13}\mathrm{d}x_Gk_{13} \\ &+ k_{14}(a_{14} - a_{14}\mathrm{d}x_G) - a_{15}(\mathrm{d}x_G - 2)k_{15} - a_{16}(\mathrm{d}x_G + 2)k_{16} \\ &- a_{17}(\mathrm{d}x_G + 1)k_{17} - a_{18}\mathrm{d}x_Gk_{18} \\ &+ k_{19}(a_{19} - a_{19}\mathrm{d}x_G) - a_2(\mathrm{d}x_G + 1)k_2 \\ &- a_{20}(\mathrm{d}x_G - 2)k_{20} - a_{21}(\mathrm{d}x_G + 2)k_{21} \\ &- a_{22}(\mathrm{d}x_G + 1)k_{22} - a_{23}\mathrm{d}x_Gk_{23} + k_{24}(a_{24} \\ &- a_{24}\mathrm{d}x_G) - a_{25}(\mathrm{d}x_G - 2)k_{25} \\ &- a_3\mathrm{d}x_Gk_3 + k_4(a_4 - a_4\mathrm{d}x_G) - a_5(\mathrm{d}x_G - 2)k_5 \\ &- a_6(\mathrm{d}x_G + 2)k_6 - a_7(\mathrm{d}x_G + 1)k_7 - a_8\mathrm{d}x_Gk_8 + k_9(a_9 \\ &- a_9\mathrm{d}x_G) + d_{x,2}q_2 + d_{x,3}q_3 + d_{x,4}q_4 + d_{x,5}q_5 + d_{x,6}q_6 \\ &+ d_{x,7}q_7 + d_{x,8}q_8 + d_{x,9}q_9 + n_{x,1}q_{10}(\lambda_* + 2\mu_*) + n_{x,2}q_{11}(\lambda_* + 2\mu_*) + n_{x,3}q_{12}(\lambda_* + 2\mu_*) + n_{x,4}q_{13}(\lambda_* + 2\mu_*) + n_{x,5}q_{14}(\lambda_* \\ &+ 2\mu_*) + n_{x,6}q_{15}(\lambda_* + 2\mu_*) + n_{x,7}q_{16}(\lambda_* + 2\mu_*) + n_{x,9}q_{18}(\lambda_* + 2\mu_*) + \lambda_*n_{y,1}q_{28} \\ &+ \lambda_*n_{y,2}q_{29} + \lambda_*n_{y,3}q_{30} + \lambda_*n_{y,4}q_{31} \\ &+ \lambda_*n_{y,5}q_{32} + \lambda_*n_{y,6}q_{33} \\ &+ \lambda_*n_{y,7}q_{34} + \lambda_*n_{y,8}q_{35} + \lambda_*n_{y,9}q_{36} \end{split}$$

$$\begin{split} b_6 &= -a_1(\mathrm{d}x_G + 2)\bar{k}_1 - a_{10}(\mathrm{d}x_G - 2)\bar{k}_{10} - a_{11}(\mathrm{d}x_G + 2)\bar{k}_{11} \\ &- a_{12}(\mathrm{d}x_G + 1)\bar{k}_{12} - a_{13}\mathrm{d}x_G\bar{k}_{13} + \bar{k}_{14}(a_{14}) \\ &- a_{14}\mathrm{d}x_G) - a_{15}(\mathrm{d}x_G - 2)\bar{k}_{15} - a_{16}(\mathrm{d}x_G + 2)\bar{k}_{16} \\ &- a_{17}(\mathrm{d}x_G + 1)\bar{k}_{17} - a_{18}\mathrm{d}x_G\bar{k}_{18} \\ &+ \bar{k}_{19}(a_{19} - a_{19}\mathrm{d}x_G) - a_2(\mathrm{d}x_G + 1)\bar{k}_2 - a_{20}(\mathrm{d}x_G - 2)\bar{k}_{20} \\ &- a_{21}(\mathrm{d}x_G + 2)\bar{k}_{21} - a_{22}(\mathrm{d}x_G + 1)\bar{k}_{22} \\ &- a_{23}\mathrm{d}x_G\bar{k}_{23} + \bar{k}_{24}(a_{24}) \\ &- a_{24}\mathrm{d}x_G) - a_{25}(\mathrm{d}x_G - 2)\bar{k}_{25} - a_3\mathrm{d}x_G\bar{k}_3 \\ &+ \bar{k}_4(a_4 - a_4\mathrm{d}x_G) - a_5(\mathrm{d}x_G - 2)\bar{k}_5 - a_6(\mathrm{d}x_G + 2)\bar{k}_6 \\ &- a_7(\mathrm{d}x_G + 1)\bar{k}_7 - a_8\mathrm{d}x_G\bar{k}_8 \\ &+ \bar{k}_9(a_9 - a_9\mathrm{d}x_G) + d_{x,2}q_{20} + d_{x,3}q_{21} \\ &+ d_{x,4}q_{22} + d_{x,5}q_{23} + d_{x,6}q_{24} \\ &+ d_{x,7}q_{25} + d_{x,8}q_{26} + d_{x,9}q_{27} + n_{x,1}\mu_*q_{28} \\ &+ n_{x,2}\mu_*q_{29} + n_{x,3}\mu_*q_{30} + n_{x,4}\mu_*q_{31} \\ &+ n_{x,5}\mu_*q_{32} + n_{x,6}\mu_*q_{33} \\ &+ n_{x,7}\mu_*q_{34} + n_{x,8}\mu_*q_{35} + n_{x,9}\mu_*q_{36} \\ &+ n_{y,1}\mu_*q_{10} + n_{y,2}\mu_*q_{11} + n_{y,3}\mu_*q_{12} \\ &+ n_{y,4}\mu_*q_{13} + n_{y,5}\mu_*q_{14} + n_{y,6}\mu_*q_{15} + n_{y,7}\mu_*q_{16} \\ &+ n_{y,8}\mu_*q_{17} + n_{y,9}\mu_*q_{18} \end{split}$$



$$\begin{aligned} b_5 &= (a_1 - 1)(\mathrm{d} C_6 + 2)k_1 + (a_0 - 1)(\mathrm{d} c_6 - 2)k_{10} \\ &+ (a_{11} - 1)(\mathrm{d} C_6 + 2)k_{11} \\ &+ (a_{12} - 1)(\mathrm{d} C_6 + 2)k_{11} \\ &+ (a_{12} - 1)(\mathrm{d} C_6 + 2)k_{11} \\ &+ (a_{12} - 1)(\mathrm{d} C_6 + 2)k_{11} \\ &+ (a_{14} - 1)(\mathrm{d} C_6 - 1)k_{12} \\ &+ (a_{14} - 1)(\mathrm{d} C_6 - 1)k_{12} \\ &+ (a_{14} - 1)(\mathrm{d} C_6 - 1)k_{12} \\ &+ (a_{16} - 1)(\mathrm{d} C_6 - 1)k_{12} \\ &+ (a_{16} - 1)(\mathrm{d} C_6 - 1)k_{12} \\ &+ (a_{11} - 1)(\mathrm{d} C_6 - 1)k_{12} \\ &+ (a_{11} - 1)(\mathrm{d} C_6 - 1)k_{21} \\ &+ (a_{12} - 1)(\mathrm{d} C_6 - 1)k_{22} \\ &+ (a_{21} - 1)(\mathrm{d} C_6 - 2)k_{21} \\ &+ (a_{21} - 1)(\mathrm{d} C_6 - 2)k_{22} \\ &+ (a_{22} - 1)(\mathrm{d} C_6 - 1)k_{2} \\ &+ (a_{21} - 1)(\mathrm{d} C_6 - 2)k_{22} \\ &+ (a_{22} - 1)(\mathrm{d} C_6 - 2)k_{22} \\$$

 $+ n_{v,7}q_{34}(\lambda_* + 2\mu_*) + n_{v,8}q_{35}(\lambda_*)$

 $+2\mu_*$) + $n_{v,9}q_{36}(\lambda_* + 2\mu_*)$



 $-n_{v,5}\mu_{**}q_{14}-n_{v,6}\mu_{**}q_{15}-n_{v,7}\mu_{**}q_{16}$

 $-n_{v.8}\mu_{**}q_{17}-n_{v.9}\mu_{**}q_{18}$

Appendix 2: The stencil coefficients for homogeneous materials

The stencils coefficients can be analytically found (see [38]) and for the first stencil they are (for convenience, the matrix form is used below for the representation of these coefficients for square meshes with $b_v = 1$):

$$\begin{pmatrix}
\bar{k}_{2,21} & \bar{k}_{2,22} & \bar{k}_{2,23} & \bar{k}_{2,24} & \bar{k}_{2,25} \\
\bar{k}_{2,16} & \bar{k}_{2,17} & \bar{k}_{2,18} & \bar{k}_{2,19} & \bar{k}_{2,20} \\
\bar{k}_{2,11} & \bar{k}_{2,12} & \bar{k}_{2,13} & \bar{k}_{2,14} & \bar{k}_{2,15} \\
\bar{k}_{2,6} & \bar{k}_{2,7} & \bar{k}_{2,8} & \bar{k}_{2,9} & \bar{k}_{2,10} \\
\bar{k}_{2,1} & \bar{k}_{2,2} & \bar{k}_{2,3} & \bar{k}_{2,4} & \bar{k}_{2,5}
\end{pmatrix} = \begin{pmatrix}
k_{1,21} & k_{1,22} & k_{1,23} & k_{1,24} & k_{1,25} \\
k_{1,16} & k_{1,17} & k_{1,18} & k_{1,19} & k_{1,20} \\
k_{1,11} & k_{1,12} & k_{1,13} & k_{1,14} & k_{1,15} \\
k_{1,6} & k_{1,7} & k_{1,8} & k_{1,9} & k_{1,10} \\
k_{1,1} & k_{1,2} & k_{1,3} & k_{1,4} & k_{1,5}
\end{pmatrix}, (43)$$

$$\begin{pmatrix} k_{1,21} & k_{1,22} & k_{1,23} & k_{1,24} & k_{1,25} \\ k_{1,16} & k_{1,17} & k_{1,18} & k_{1,16} & k_{1,17} \\ k_{1,16} & k_{1,17} & k_{1,18} & k_{1,16} \\ k_{1,17} & k_{1,18} & k_{1,16} & k_{1,17} \\ k_{1,16} & k_{1,17} & k_{1,18} & k_{1,16} \\ k_{1,17} & k_{1,18} & k_{1,16} & k_{1,17} \\ k_{1,16} & k_{1,17} & k_{1,18} & k_{1,16} \\ k_{1,1} & k_{1,2} & k_{1,3} & k_{1,4} & k_{1,15} \\ k_{1,6} & k_{1,7} & k_{1,8} & k_{1,9} & k_{1,10} \\ k_{1,1} & k_{1,2} & k_{1,3} & k_{1,4} & k_{1,15} \\ k_{1,6} & k_{1,7} & k_{1,8} & k_{1,9} & k_{1,10} \\ k_{1,1} & k_{1,2} & k_{1,3} & k_{1,4} & k_{1,15} \\ k_{1,6} & k_{1,7} & k_{1,8} & k_{1,9} & k_{1,10} \\ k_{1,1} & k_{1,2} & k_{1,3} & k_{1,4} & k_{1,5} \\ k_{1,6} & k_{1,7} & k_{1,8} & k_{1,9} & k_{1,10} \\ k_{1,1} & k_{1,2} & k_{1,8} & k_{1,9} & k_{1,10} \\ k_{1,1} & k_{1,2} & k_{1,8} & k_{1,9} & k_{1,10} \\ k_{1,1} & k_{1,2} & k_{1,8} & k_{1,4} & k_{1,15} \\ k_{1,6} & k_{1,7} & k_{1,8} & k_{1,9} & k_{1,10} \\ k_{1,1} & k_{1,2} & k_{1,3} & k_{1,4} & k_{1,15} \\ k_{1,6} & k_{1,7} & k_{1,8} & k_{1,9} & k_{1,10} \\ k_{1,1} & k_{1,2} & k_{1,1} & k_{1,15} \\ k_{1,6} & k_{1,7} & k_{1,8} & k_{1,9} & k_{1,10} \\ k_{1,1} & k_{1,2} & k_{1,2} & k_{1,2} & k_{1,2} \\ k_{1,1} & k_{1,1} & k_{1,15} \\ k_{1,6} & k_{1,7} & k_{1,8} & k_{1,9} & k_{1,10} \\ k_{1,1} & k_{1,2} & k_{1,1} & k_{1,15} \\ k_{1,6} & k_{1,7} & k_{1,8} & k_{1,9} & k_{1,10} \\ k_{1,1} & k_{1,2} & k_{1,3} & k_{1,4} & k_{1,15} \\ k_{1,1} & k_{1,1} & k_{1,15} & k_{1,15} \\ k_{1,1} & k_{1,1} & k_{1,1} & k_{1,1} \\ k_{1,1} & k_{1,1} & k_{1,1} & k_{1,15} \\ k_{1,1} & k_$$

Similarly, we can find 50 coefficients $k_{2,i}$ and $\bar{k}_{2,i}$ (i = 1, 2, ..., 25) of the second stencil equation:

$$\begin{pmatrix} k_{2,21} & k_{2,22} & k_{2,23} & k_{2,24} & k_{2,25} \\ k_{2,16} & k_{2,17} & k_{2,18} & k_{2,19} & k_{2,20} \\ k_{2,11} & k_{2,12} & k_{2,13} & k_{2,14} & k_{2,15} \\ k_{2,6} & k_{2,7} & k_{2,8} & k_{2,9} & k_{2,10} \\ k_{2,1} & k_{2,2} & k_{2,3} & k_{2,4} & k_{2,5} \end{pmatrix} = \begin{pmatrix} \bar{k}_{1,21} & \bar{k}_{1,22} & \bar{k}_{1,23} & \bar{k}_{1,24} & \bar{k}_{1,25} \\ \bar{k}_{1,16} & \bar{k}_{1,17} & \bar{k}_{1,18} & \bar{k}_{1,19} & \bar{k}_{1,20} \\ \bar{k}_{1,11} & \bar{k}_{1,12} & \bar{k}_{1,13} & \bar{k}_{1,14} & \bar{k}_{1,15} \\ \bar{k}_{1,6} & \bar{k}_{1,7} & \bar{k}_{1,8} & \bar{k}_{1,9} & \bar{k}_{1,10} \\ \bar{k}_{1,1} & \bar{k}_{1,2} & \bar{k}_{1,3} & \bar{k}_{1,4} & \bar{k}_{1,5} \end{pmatrix}^{T},$$

$$(42)$$

where the right-hand sides in Eqs. (42) and (43) are given by Eqs. (40) and (41) for the first stencil.



Appendix 3: The expression for the term p_1 in Eqs. (28) and (29)

$$\begin{split} p_1 &= (a_{10}k_{10}(\mathrm{dx}_G - 2)^2 + a_{1}(\mathrm{dx}_G + 2)^2k_1 \\ &\quad + a_{11}\mathrm{dx}_G^2k_{11} + 4a_{11}k_{11} \\ &\quad + 4a_{11}\mathrm{dx}_Gk_{11} + a_{12}\mathrm{dx}_G^2k_{12} + a_{12}k_{12} + 2a_{12}\mathrm{dx}_Gk_{12} \\ &\quad + a_{13}\mathrm{dx}_G^2k_{13} + a_{14}\mathrm{dx}_G^2k_{14} + a_{14}k_{14} \\ &\quad - 2a_{14}\mathrm{dx}_Gk_{14} + a_{15}\mathrm{dx}_G^2k_{15} \\ &\quad + 4a_{15}k_{15} - 4a_{15}\mathrm{dx}_Gk_{15} \\ &\quad + a_{16}\mathrm{dx}_G^2k_{16} + 4a_{16}k_{16} + 4a_{16}\mathrm{dx}_Gk_{16} \\ &\quad + a_{17}\mathrm{dx}_Gk_{17} + a_{17}k_{17} \\ &\quad + 2a_{17}\mathrm{dx}_Gk_{17} + a_{18}\mathrm{dx}_G^2k_{18} \\ &\quad + a_{19}\mathrm{dx}_G^2k_{19} + a_{19}k_{19} - 2a_{19}\mathrm{dx}_Gk_{19} \\ &\quad + a_{20}\mathrm{dx}_G^2k_{2} + a_{20}\mathrm{dx}_G^2k_{20} + 4a_{20}k_{20} - 4a_{20}\mathrm{dx}_Gk_{20} \\ &\quad + a_{21}\mathrm{dx}_G^2k_{21} + 4a_{21}k_{21} \\ &\quad + 4a_{21}\mathrm{dx}_Gk_{21} + a_{22}\mathrm{dx}_G^2k_{22} + a_{22}k_{22} \\ &\quad + 2a_{22}\mathrm{dx}_Gk_{22} + a_{23}\mathrm{dx}_G^2k_{23} + a_{24}\mathrm{dx}_G^2k_{24} \\ &\quad + a_{24}k_{24} - 2a_{24}\mathrm{dx}_Gk_{24} \\ &\quad + a_{25}\mathrm{dx}_G^2k_{25} + 4a_{25}k_{25} - 4a_{25}\mathrm{dx}_Gk_{25} + a_{3}\mathrm{dx}_G^2k_{3} \\ &\quad + a_{40}\mathrm{dx}_G^2k_{4} + a_{4k} - 2a_{4}\mathrm{dx}_Gk_{4} + a_{5}\mathrm{dx}_G^2k_{5} \\ &\quad + 4a_{6}\mathrm{dx}_Gk_{6} + 4a_{6}k_{6} \\ &\quad + 4a_{6}\mathrm{dx}_Gk_{6} + a_{7}\mathrm{dx}_G^2k_{7} + a_{7}k_{7} \\ &\quad + 2a_{7}\mathrm{dx}_Gk_{7} + a_{8}\mathrm{dx}_G^2k_{8} \\ &\quad + a_{9}\mathrm{dx}_G^2k_{9} + a_{9}k_{9} - 2a_{9}\mathrm{dx}_Gk_{9} \\ &\quad + 2d_{x,2}\lambda_{*}n_{x,2}q_{11} + 4d_{x,2}n_{x,2}\mu_{*}q_{11} \\ &\quad + 2d_{x,3}\lambda_{*}n_{x,3}q_{12} \\ &\quad + 4d_{x,6}n_{x,6}\mu_{*}q_{13} + 2d_{x,5}\lambda_{*}n_{x,5}q_{14} \\ &\quad + 4d_{x,6}n_{x,6}\mu_{*}q_{15} + 2d_{x,7}\lambda_{*}n_{x,7}q_{16} \\ &\quad + 4d_{x,7}n_{x,7}\mu_{*}q_{16} \\ &\quad + 2d_{x,3}\lambda_{*}n_{x,3}q_{30} + 2d_{x,4}\lambda_{*}n_{y,4}q_{31} \\ &\quad + 2d_{x,3}\lambda_{*}n_{y,3}q_{30} + 2d_{x,4}\lambda_{*}n_{y,9}q_{33} \\ &\quad + 2d_{x,3}\lambda_{*}n_{y,9}q_{36} + 2d_{x,4}\lambda_{*}n_{y,9}q_{33} \\ &\quad + 2d_{x,3}\lambda_{*}n_{y,9}q_{36} + 2d_{x,4}\lambda_{*}n_{y,9}q_{33} \\ &\quad + 2d_{x,3}\lambda_{*}n_{y,9}q_{36} + d_{x,4}^2q_{4} + d_{x,5}^2q_{5} + d_{x,6}^2q_{6} \\ \end{aligned}$$



Acknowledgements The research of AI (theoretical developments) and as well as BD and MM (numerical study) has been supported in part by the Army Research Office (Grant number W911NF-21-1-0267), the NSF Grant CMMI-1935452 and by Texas Tech University. The views and conclusions contained in this paper are those of the authors and should not be interpreted as representing the official policies.

References

(44)

- Singh K, Williams J (2005) A parallel fictitious domain multigrid preconditioner for the solution of Poisson's equation in complex geometries. Comput Methods Appl Mech Eng 194(45-47):4845-4860
- Vos P, van Loon R, Sherwin S (2008) A comparison of fictitious domain methods appropriate for spectral/hp element discretisations. Comput Methods Appl Mech Eng 197(25–28):2275–2289
- Burman E, Hansbo P (2010) Fictitious domain finite element methods using cut elements: I. A stabilized Lagrange multiplier method. Comput Methods Appl Mech Eng 199(41–44):2680–2686
- Rank E, Kollmannsberger S, Sorger C, Duster A (2011) Shell finite cell method: a high order fictitious domain approach for thin-walled structures. Comput Methods Appl Mech Eng 200(45–46):3200–3209
- Rank E, Ruess M, Kollmannsberger S, Schillinger D, Duster A (2012) Geometric modeling, isogeometric analysis and the finite cell method. Comput Methods Appl Mech Eng 249–252:104–115
- Fries T, Omerović S, Schöllhammer D, Steidl J (2017) Higherorder meshing of implicit geometries-part I: integration and interpolation in cut elements. Comput Methods Appl Mech Eng 313:759–784
- Hoang T, Verhoosel CV, Auricchio F, van Brummelen EH, Reali A (2017) Mixed isogeometric finite cell methods for the stokes problem. Comput Methods Appl Mech Eng 316:400–423
- Zhao S, Wei GW (2009) Matched interface and boundary (MIB) for the implementation of boundary conditions in highorder central finite differences. Int J Numer Methods Eng 77(12):1690–1730
- May S, Berger M (2017) An explicit implicit scheme for cut cells in embedded boundary meshes. J Sci Comput 71(3):919–943
- Kreisst H-O, Petersson NA (2006) An embedded boundary method for the wave equation with discontinuous coefficients. SIAM J Sci Comput 28(6):2054–2074
- Kreiss H-O, Petersson NA (2006) A second order accurate embedded boundary method for the wave equation with Dirichlet data. SIAM J Sci Comput 27(4):1141–1167
- Kreiss H-O, Petersson NA, Ystrom J (2004) Difference approximations of the Neumann problem for the second order wave equation. SIAM J Numer Anal 42(3):1292–1323
- Jomaa Z, Macaskill C (2010) The Shortley–Weller embedded finite-difference method for the 3D Poisson equation with mixed boundary conditions. J Comput Phys 229(10):3675–3690
- Jomaa Z, Macaskill C (2005) The embedded finite difference method for the Poisson equation in a domain with an irregular boundary and Dirichlet boundary conditions. J Comput Phys 202(2):488–506
- Hellrung JL Jr, Wang L, Sifakis E, Teran JM (2012) A second order virtual node method for elliptic problems with interfaces and irregular domains in three dimensions. J Comput Phys 231(4):2015–2048



 $+d_{r_{1}}^{2}q_{7}+d_{r_{8}}^{2}q_{8}+d_{r_{9}}^{2}q_{9}$).

- Chen L, Wei H, Wen M (2017) An interface-fitted mesh generator and virtual element methods for elliptic interface problems. J Comput Phys 334:327–348
- Bedrossian J, von Brecht JH, Zhu S, Sifakis E, Teran JM (2010) A second order virtual node method for elliptic problems with interfaces and irregular domains. J Comput Phys 229(18):6405–6426
- Assêncio DC, Teran JM (2013) A second order virtual node algorithm for stokes flow problems with interfacial forces, discontinuous material properties and irregular domains. J Comput Phys 250:77–105
- Mattsson K, Almquist M (2017) A high-order accurate embedded boundary method for first order hyperbolic equations. J Comput Phys 334:255–279
- Schwartz P, Barad M, Colella P, Ligocki T (2006) A Cartesian grid embedded boundary method for the heat equation and Poisson's equation in three dimensions. J Comput Phys 211(2):531–550
- Dakin G, Despres B, Jaouen S (2018) Inverse Lax-Wendroff boundary treatment for compressible Lagrange-remap hydrodynamics on Cartesian grids. J Comput Phys 353:228–257
- Colella P, Graves DT, Keen BJ, Modiano D (2006) A Cartesian grid embedded boundary method for hyperbolic conservation laws. J Comput Phys 211(1):347–366
- Crockett R, Colella P, Graves D (2011) A Cartesian grid embedded boundary method for solving the Poisson and heat equations with discontinuous coefficients in three dimensions. J Comput Phys 230(7):2451–2469
- McCorquodale P, Colella P, Johansen H (2001) A Cartesian grid embedded boundary method for the heat equation on irregular domains. J Comput Phys 173(2):620–635
- Johansen H, Colella P (1998) A Cartesian grid embedded boundary method for Poisson's equation on irregular domains. J Comput Phys 147(1):60–85
- Angel JB, Banks JW, Henshaw WD (2018) High-order upwind schemes for the wave equation on overlapping grids: Maxwell's equations in second-order form. J Comput Phys 352:534–567
- Uddin H, Kramer R, Pantano C (2014) A Cartesian-based embedded geometry technique with adaptive high-order finite differences for compressible flow around complex geometries. J Comput Phys 262:379–407
- Main A, Scovazzi G (2018) The shifted boundary method for embedded domain computations. part I: Poisson and Stokes problems. J Comput Phys 372:972–995
- Song T, Main A, Scovazzi G, Ricchiuto M (2018) The shifted boundary method for hyperbolic systems: embedded domain computations of linear waves and shallow water flows. J Comput Phys 369:45–79
- Hosseinverdi S, Fasel HF (2018) An efficient, high-order method for solving Poisson equation for immersed boundaries: combination of compact difference and multiscale multigrid methods. J Comput Phys 374:912–940
- Zhang Q, Babuska I (2020) A stable generalized finite element method (SGFEM) of degree two for interface problems. Comput Methods Appl Mech Eng 363:112889
- Guo R, Lin T, Lin Y (2019) Approximation capabilities of immersed finite element spaces for elasticity interface problems. Numer Methods Partial Differ Equ 35(3):1243–1268
- Yu S, Wei G (2007) Three-dimensional matched interface and boundary (MIB) method for treating geometric singularities. J Comput Phys 227(1):602–632

- Huang T-H, Chen J-S, Tupek MR, Beckwith FN, Koester JJ, Fang HE (2021) A variational multiscale immersed meshfree method for heterogeneous materials. Comput Mech 67:1059–1097
- 35. Idesman A (2020) A new numerical approach to the solution of PDEs with optimal accuracy on irregular domains and Cartesian meshes. Part 1: the derivations for the wave heat and Poisson equations in the 1-D and 2-D cases. Arch Appl Mech 90(12):2621–2648
- Dey B, Idesman A (2020) A new numerical approach to the solution of PDEs with optimal accuracy on irregular domains and Cartesian meshes. Part 2: numerical simulation and comparison with FEM. Arch Appl Mech 90(12):2649–2674
- Idesman A, Dey B (2019) A new 3-D numerical approach to the solution of PDEs with optimal accuracy on irregular domains and Cartesian meshes. Comput Methods Appl Mech Eng 354:568–592
- Idesman A, Dey B (2020) Compact high-order stencils with optimal accuracy for numerical solutions of 2-D time-independent elasticity equations. Comput Methods Appl Mech Eng 360:1–17
- Idesman A, Dey B (2020) Accurate numerical solutions of 2-D elastodynamics problems using compact high-order stencils. Comput Struct 229:1–18
- Idesman A, Dey B (2020) A new numerical approach to the solution of the 2-D Helmholtz equation with optimal accuracy on irregular domains and Cartesian meshes. Comput Mech 65:1189–1204
- 41. Idesman A, Dey B (2020) New 25-point stencils with optimal accuracy for 2-d heat transfer problems. Comparison with the quadratic isogeometric elements. J Comput Phys 418:109640
- Idesman A, Dey B (2021) Optimal local truncation error method for solution of wave and heat equations for heterogeneous materials with irregular interfaces and unfitted Cartesian meshes. Comput Methods Appl Mech Eng 384:113998
- 43. Idesman A, Dey B (2020) The treatment of the Neumann boundary conditions for a new numerical approach to the solution of PDEs with optimal accuracy on irregular domains and Cartesian meshes. Comput Methods Appl Mech Eng 365:112985
- 44. Idesman A, Mobin M (2022) Optimal local truncation error method for solution of 3-D Poisson equation with irregular interfaces and unfitted Cartesian meshes as well as for post-processing. Adv Eng Softw 167:103103
- Bathe KJ (1996) Finite element procedures. Prentice-Hall Inc., Upper Saddle River
- Langtangen HP, Linge S (2017) Finite difference computing with PDEs. Springer, Berlin
- Lin T, Sheen D, Zhang X (2013) A locking-free immersed finite element method for planar elasticity interface problems. J Comput Phys 247:228–247
- Idesman A (2018) The use of the local truncation error to improve arbitrary-order finite elements for the linear wave and heat equations. Comput Methods Appl Mech Eng 334:268–312

Publisher's Note Springer Nature remains neutral with regard to jurisdictional claims in published maps and institutional affiliations.

